Stochastic and deterministic dynamics of intrinsically irregular firing in cortical inhibitory interneurons

Philipe R.F. Mendonça[1], Mariana Vargas-Caballero[3], Ferenc Erdélyi[2], Gábor Szabó[2], Ole Paulsen[1] and Hugh P.C. Robinson[1],

[1]Dept. of Physiology, Development and Neuroscience, University of Cambridge

[2]Division of Medical Gene Technology, Institute of Experimental Medicine, Budapest

[3]Institute for Life Sciences and Centre for Biological Sciences, University of Southampton

Summary

Most cortical neurons fire regularly when excited by a constant stimulus. In contrast, irregular-spiking (IS) interneurons are remarkable for the intrinsic variability of their spike timing, which can synchronize amongst IS cells via specific gap junctions. Here, we have studied the biophysical mechanisms of this irregular spiking in mice, and how IS cells fire in the context of synchronous network oscillations. Using patch-clamp recordings, artificial dynamic conductance injection, pharmacological analysis and computational modelling, we show that spike time irregularity is generated by a nonlinear dynamical interaction of voltage-dependent sodium and fast-inactivating potassium channels just below spike threshold, amplifying channel noise. This *active irregularity* may help IS cells synchronize with each other at gamma range frequencies, while resisting synchronization to lower input frequencies.

Running Title: Stochastic and deterministic mechanism of irregular spiking

HIGHLIGHTS

- The mechanism of irregular spiking (IS) in cortical interneurons is elucidated
- Irregular interspike intervals in IS interneurons show recurrent, deterministic patterns
- IS interneurons express persistent sodium and fast transient (A-type) potassium conductances
- Interaction of voltage-dependent conductances near threshold amplifies stochastic fluctuations and leads to irregular spike intervals
- A conductance-based computational model captured the properties of irregular spiking

INTRODUCTION

From the Hodgkin and Huxley model onwards, we have a good understanding of the dynamical basis of regular or periodic firing, and of various kinds of burst firing (FitzHugh, 1961; Hindmarsh and Rose, 1984; Hodgkin and Huxley, 1952). In contrast, the nature of intrinsically irregular firing has resisted elucidation, and appears to be a more complex phenomenon. Irregularity of firing in neurons can arise because of fluctuating patterns of synaptic input due to spontaneous activity (Destexhe et al., 2001), or from stochastic fluctuations in the release of transmitter (Ribrault et al., 2011). In some regions of the brain, though, certain types of neuron show strikingly high irregularity of firing even when isolated *in vitro* (Cauli et al., 1997; Grace and Bunney, 1984; Ascoli et al., 2008). The cellular mechanisms of such intrinsic irregularity are unknown, though stochastic gating of the ion channels involved in spike generation seems likely to play a part. Effective chaos in the nonlinear dynamics of the voltage-dependent ion channels involved in spike generation could also contribute to irregular patterns of membrane potential (Durstewitz and Gabriel, 2007; Fan and Chay, 1994).

In the cortex, the function of intrinsically irregular firing is of particular interest. Within the neural circuitry of the neocortex are various types of inhibitory interneuron, several of which have been implicated in the generation of distinct synchronous oscillations at various frequencies from slow (< 1 Hz) to very fast (> 100 Hz), such as the theta (4-10 Hz), beta (10-30 Hz) and gamma (30 – 80 Hz) oscillations (Buszsaki, 2006). For example, the fast-spiking (FS, parvalbumin-expressing, basket morphology) cell network has a crucial role in the emergence of the gamma rhythm (Cardin et al., 2009; Hasenstaub et al., 2005). Recent

evidence suggests the possibility of a similar specific role for the low-threshold-spiking (LTS, somatostatin-positive, Martinotti) cell network in lower frequency theta or beta rhythms (Fanselow et al., 2008; Vierling-Claassen et al., 2010). One type of interneuron, however, is distinguished by its intrinsically irregular repetitive firing, showing a broad, apparently random dispersion of its interspike intervals, as opposed to bursting, even when pharmacologically disconnected from any synaptic input. These irregular-spiking (IS) neurons (Cauli et al., 1997) seem to have both a distinctive mechanism of spike timing control, and possibly a unique role during synchronous network oscillations.

To enable specific targeting of IS cells, we used a mouse line with green fluorescent protein (GFP) linked to the promoter for *Gad2* (Lopez-Bendito et al., 2004), in which fluorescently labelled neurons in somatosensory cortex predominantly have an IS phenotype (Galarreta et al., 2004). These cells express CCK, VIP and 5HT3a receptors (Sugino et al., 2006). They are concentrated in layer 2 (Lopez-Bendito et al., 2004), and derive primarily from the caudal ganglionic eminence during development (Lopez-Bendito et al., 2004; Lee et al., 2010). They connect specifically to each other by gap junctions and mutually inhibitory synaptic connections, which together enable precisely-synchronized irregular firing (Galarreta et al., 2004). Their wide axonal arborizations through many layers of the cortex and inhibition of pyramidal cells (Galarreta et al., 2004, 2008) suggest that they could exert a powerful influence on the network. Another distinctive property of these cells is their expression of CB1 cannabinoid receptors, which can suppress their inhibitory output to pyramidal cells, following depolarization of the postsynaptic cell (Galarreta et al., 2008). Although they make up a large proportion of inhibitory interneurons in superficial layers, they have received much less attention than other classes of interneurons, such as FS and LTS cells.

In this study, we ask: what mechanisms underlie the striking irregularity of firing, and what are the functional consequences of this in an oscillating cortical network? Using a combination of patch-clamp recording in slices of somatosensory cortex, time series analysis and computational modelling, we show that IS neurons generate robust, intrinsically irregular firing by nonlinear interactions of voltage-dependent currents and channel noise. The degree of irregularity is tuned by the level of a fast-inactivating potassium conductance, and voltage-dependent sodium and potassium channel openings contribute a high level of voltage noise at threshold. The effect of these mechanisms is that these cells reject synchronization to a low

frequency (10 Hz), while synchronizing effectively to higher, gamma frequencies, a property which could give them a prominent role in gating local cortical gamma oscillations.

RESULTS

A genetically-defined population of irregular-spiking cortical interneurons

In the cortex of *Gad2*-GFP mice, fluorescent cell bodies are concentrated in layer 2, with dendrites concentrated in layers 1 and 2/3 and axons which ramify through the cortical layers (Figure 1a). The morphology of fluorescent neurons was varied, with bitufted, bipolar and multipolar cells observed, as described by Galarreta and Hestrin (2004). Cells had input resistances of 331±164 MΩ and passive time constants of 15.4±7.7 ms (mean ± SD, n=82). In response to a step current stimulus in a whole-cell current-clamp recording, 77% (82/106) of the cells showed a characteristic pattern of action potentials (APs) at irregular intervals, with fairly deep and slow afterhyperpolarizations, often following an initial adaptation phase (Figure 1b*i*). Irregular spiking interneurons displayed larger somata (≈15 µm diameter) and more prominent projections than did the remaining 23% of GFP+ neurons, which had a regular-spiking response (excluded from analysis, except when stated), as described by Galarreta et al. (2004, 2008).

The irregular trajectory of action potential intervals in IS neurons varied from trial to trial (Figure 1bii), and the membrane potential showed quite large, variable fluctuations between spikes (Figure 1c). Over long periods of continuous stimulation, the distribution of interspike intervals was skewed and unimodal, and could be reasonably well-fitted by a gamma function (Figure 1d). Irregularity was quantified as the coefficient of variation of interspike intervals or CV(ISI), the ratio of the standard deviation of intervals to their mean (see Materials and methods), which is equal to 1 for a Poisson point process, and 0 for a perfectly periodic process. CV(ISI) was reduced at higher stimulus levels and firing frequencies, and was quite variable from cell to cell, but ranged from 0.1 (fairly regular) to 0.6 at a firing frequency of ≈10 Hz (CV_{10Hz} = 0.28±0.15, n = 45). The irregularity persisted in the presence of blockers of ionotropic glutamate and $GABA_A$ receptors and is therefore presumably generated intrinsically, rather than by noisy synaptic input. The intrinsic nature of the IS was confirmed in primary cultures of dissociated *Gad2* neurons, which displayed a similar spiking pattern, despite simpler morphology and reduced connectivity (Figure 1e,f).

Recurrence of sequences of irregular interspike intervals

To characterize the dynamics of irregular spiking, we first examined return maps of interspike intervals – scatter plots of each interval against its successor – which displayed no discernible fine structure (Figure 2a, b). We therefore looked at the predictability of higher-order sequences of intervals using recurrence plots (Eckmann et al., 1987; Marwan et al., 2007). First, sequences of interspike intervals were embedded – that is, translated into all sub-sequences of length m, the embedding dimension – each of which defines a point in m-dimensional embedding space, and can be thought of as a piece of "recent history". For example, Figure 2c (top) illustrates two similar embedding points of dimension m=3 occurring within two different interval sequences. Similarity of dynamical state is measured by proximity in this space (Figure 2c, bottom), and this can be generalized to any m. A cross-recurrence plot of two sequences of intervals, A and B, for example two successive spiking responses to an identical step current stimulus, is a matrix in which element (i,j) has a value representing the distance between the ith embedding point of A and the jth embedding point of B, or zero if not (Eckmann et al., 1987; Marwan et al., 2007) (see Materials and methods for further details). Figure 2e shows an example in which Euclidean distance in embedding space is represented by color, so that close recurrences show up as coloured dots on a grey background. Diagonal lines of slope one, many examples of which can be seen in Figure 2e, indicate periods when the trajectory of one time series evolves similarly to the trajectory of the other. Examples of four different recurrent ISI sequence "motifs", identified from the recurrence plot in Figure 2e, are shown in Figure 2f. Recurrence can be quantified as follows. Applying a threshold to the cross-recurrence plot, so that element (i,j) = 1 if the distance between i and j is less than a threshold neighbourhood size ε (see Figure 2d), or zero otherwise, gives a binary cross-recurrence plot, in which the density of 1's is defined as the degree of recurrence, and the fraction of these which lie within diagonals of length 2 or greater is defined as the degree of determinism. Randomly shuffling the time series before embedding destroys significant recurrence and determinism (allowing statistical testing of their significance (see Figure 2 – figure supplement 1, and Materials and methods). We calculated cross-recurrence plots between successive pairs of trials (5-30 s in duration), omitting the first 450 ms of firing in each trial to exclude initial adaptation, for 10 neurons which showed long periods of stationary responses (Figure 2d), at average firing frequencies between 4 and 17 Hz. Using a standard sequence size or embedding dimension m = 4, and a

155 neighbourhood size (ε) of one standard deviation of the ISIs, we found that in five of ten cells,
156 both recurrence and determinism were significant ($p < 0.05$, z-test), while only recurrence was
157 significant in a further two cells, and in the three remaining cells, neither recurrence nor
158 determinism were significant. See Figure 2 – source data 2 for details. Note that, unlike the
159 related technique of nonlinear prediction (Kantz and Schreiber, 1997), the detection of
160 significant recurrence and dynamical determinism is less confounded by nonstationarity, and
161 relatively insensitive to the exact choice of *m* and ε. Thus, irregular sequences of spikes
162 generated during a constant stimulus in about half of IS neurons show recurrent, correlated
163 sequences of four or more successive intervals. It seems likely that the concerted action of
164 voltage-dependent ion channel populations would be involved in producing such determinism.
165 We found similar recurrence and determinism in a conductance-based biophysical model of
166 these cells, described below, when applying the same analysis procedure to its spike trains
167 (Figure 6, Figure 6 – figure supplement 1). We noted that those cells that failed to show
168 significant recurrence and determinism had particularly strong voltage noise in their
169 interspike intervals (not shown).

170

171 **Voltage-dependent sodium channel openings are required for voltage fluctuations**

172 Next, we investigated the biophysical mechanisms which underlie the irregular firing. Clearly,
173 one potentially relevant phenomenon is the noisy fluctuation in membrane potential which
174 switches on above -50 mV (Figure 3a). We found that these fluctuations depended on
175 voltage-gated sodium channels, since they were eliminated by applying tetrodotoxin (TTX;
176 Figure 3b, n = 6 cells). To further investigate the unitary properties of voltage-gated sodium
177 channels, we carried out cell-attached recordings in somatic patches. Characteristic ≈20 pS
178 inward openings were observed, concentrated soon after the beginning of the depolarization
179 (Figure 3c), with an extrapolated reversal potential of about +120 mV positive to the resting
180 potential, as expected for single voltage-gated sodium channels (Sigworth and Neher, 1980).
181 We also observed frequent late openings of the same channel amplitude, up to 100 ms
182 following +40 mV depolarizations from rest, (Figure 3c and d, in 4 out of 5 patches
183 containing transient Na channels). Whole-cell recordings further confirmed the presence of a
184 non-inactivating, TTX sensitive inward current, evoked in response to a slowly depolarizing
185 ramp (Figure 3e, prominent in 11/13 cells), when K^+ and Ca^{2+} currents were reduced with
186 TEA (2 mM), 4-AP (2 mM) and Cd^{2+} (200 μM). Similar "persistent" sodium current (NaP)
187 and channel openings have been described in many neurons and excitable cells (Kiss, 2008).

188 Thus, stochastic, voltage-dependent gating of sodium channels could be involved in
189 generating irregularity of firing. Sodium-channel-driven subthreshold noise has been
190 observed in other cell types (White et al., 1998), but without appearing to produce the high
191 level of firing irregularity observed in IS cells at ≈10 Hz firing frequencies (Alonso and Klink,
192 1993). The deterministic recurrence of the interspike intervals suggests that another active
193 mechanism might also be involved.

194

195 **A fast-inactivating potassium current activates around threshold**

196 Both voltage-gated and calcium-activated potassium channels contribute to spike
197 repolarization and spike afterhyperpolarizations in cortical neurons. However, neither
198 blockers of calcium-activated potassium channels (iberiotoxin and apamin) nor intracellular
199 perfusion of a fast calcium buffer (BAPTA) diminished irregularity of firing (see Figure 4 –
200 figure supplement 1), and we concluded that intracellular calcium signalling is not centrally
201 involved in the dynamics of intrinsic irregularity. We therefore next examined the voltage-
202 dependent potassium currents, which are of key importance in determining action potential
203 generation and shape (Bean, 2007). In particular, we focussed on those whose voltage-
204 dependence of gating might allow dynamical interaction with the sodium channels.

205 Whole-cell voltage-clamp of the outward currents in response to families of step
206 depolarizations revealed an early transient outward or A-type potassium current (Figure 4a),
207 which could be isolated by applying a pre-pulse protocol (Amarillo et al., 2008, Maffie et al.,
208 2013) in the presence of 5 mM TEA to remove slower K^+ currents (Figure 4b, n=9). Fits of
209 the voltage-dependence of the peak conductance and of the steady-state inactivation of this
210 transient potassium conductance (g_{Kt}) showed that activation and inactivation curves
211 overlapped around the threshold (Figure 4c, n=18 cells for inactivation, n=36 cells for
212 activation), peaking within 1-2 ms, and inactivating over about 20-30 ms (Figure 4d, top).
213 Additionally, this fast inactivating outward current recovered from inactivation with a time
214 constant of around 40 ms at -70 mV (Figure 4d, bottom). These properties are not consistent
215 with Kv1 channels (the current was insensitive to 1 μM α-dendrotoxin, n=4, not shown),
216 including Kv1.4 (recovery from inactivation in the range of milliseconds rather than seconds,
217 see Wickenden et al., 1999), nor with channels from the Kv3 family (transient currents were
218 TEA insensitive, see Figure 4 – figure supplement 2). The gating properties closely resemble
219 those of Kv4-family voltage-dependent potassium channels in pyramidal neurons (Birnbaum

220 et al., 2004), and this was further supported by its sensitivity to 4-AP (Figure 4e top, n=6) and
221 the specific Kv4.2/4.3 blocker phrixotoxin (PhTX; Figure 4e bottom, n=7), which produced a
222 partial, reversible block of 55% at a concentration of 5 μM. We fitted conventional Hodgkin-
223 Huxley type models to the voltage-step responses of this current (see Materials and methods),
224 and estimated a peak transient conductance at 0 mV (g_{max0}, see Materials and methods) of
225 22.37 ± 14.41 nS (n = 8 cells, mean ± SD). This current would be expected to delay the rise
226 of membrane potential just before spike initiation. Although the membrane potential leading
227 into spikes was generally highly fluctuating, averaging the waveform of hundreds of action
228 potential, aligned by the fastest point of the upstroke, consistently showed the presence of a
229 clear dip or inflexion in the rising phase, about 10 ms before the start of the fast upstroke
230 (Figure 4f), which we attribute to this current. There was also a high density of single channel
231 currents in some cell-attached patches (n=7), with similar activation and inactivation
232 properties (Figure 4g and 4h), implying some clustering in the membrane, as previously
233 described for Kv4 channels (Alonso and Widmer, 1997; Jinno et al., 2005). The fast and
234 small-amplitude single channel openings in these recordings were not well-resolved, but
235 appeared to comprise step transitions corresponding to a single channel chord conductance of
236 about 10-12 pS (assuming $E_K \approx$ -90 mV). The single channel conductance of Kv4 channels is
237 not extensively-characterised, but reports vary from ≈5 pS to ≈20 pS in low potassium
238 external solutions, and it is sensitive both to external potassium concentration and to
239 association with accessory proteins such as KChIPs (Holmquist et al., 2002; Cooper and
240 Shrier, 1999). Thus, overall, the transient potassium conductance recorded at the soma
241 strongly resembles reported descriptions of Kv4-mediated conductance.

242 **Transient outward conductance determines spike irregularity**

243 To test whether and how this inactivating K^+ current is involved in generating irregular firing,
244 we injected a synthetic dynamic conductance (Robinson and Kawai, 1993; Sharp et al., 1993)
245 with the kinetics and voltage-dependence measured from voltage clamp, which should have
246 the same electrical effect as the native conductance at the soma. Artificial conductance
247 injection of g_{Kt} was sufficient to modulate the spiking irregularity of intrinsically irregular
248 *Gad2* interneurons (Figure 5a, b and c, Figure 5 – figure supplement 2). When negative g_{Kt}
249 was injected, i.e. *subtracting* from the dynamics of the native conductance in these cells (as
250 shown in Figure 5d for voltage clamp currents), we saw a striking regularisation of firing in
251 the range of frequency examined, as well as a reduction in the afterhyperpolarization (AHP)
252 amplitude. On the other hand, injecting positive g_{Kt} induced an increase in the irregularity of

253 firing, accompanied by a more prominent subthreshold membrane potential fluctuation
254 between spikes (Figure 5c). The effect of g_{Kt} on CV(ISI) was consistent especially at lower
255 firing frequencies (e.g. 10 Hz, figure 5e, n=42 cells), and it was even more evident when the
256 total g_{Kt} injected was normalized to the capacitance of each cell, which is related to its
257 plasma membrane area (Figure 5f). Pharmacological block of g_{Kt} by 4-AP or phrixotoxin
258 gave a similar result to negative conductance injection, reducing irregularity of firing (See
259 Figure 5 – figure supplement 3).

260 **Mechanisms of firing variability in a simple model of IS neurons**

261 Having shown experimentally that the transient potassium current plays a key role in
262 controlling irregular firing in IS neurons, we sought to understand how it might do so, by
263 studying a computational model of these cells. We constructed a conductance-based
264 biophysical model, in which the key g_{Kt} and NaP conductances could be modelled either as
265 stochastic or deterministic elements. A two-compartment model was used, comprising a
266 somatic compartment which contained voltage-dependent conductances, linked to a passive
267 dendritic compartment. The dendritic compartment was included in order to capture, in a
268 simplified way, the extended spatial aspect of the cell morphology. Similarly to a widely-
269 used model of fast-spiking inhibitory interneurons (Erisir et al., 1999; Gouwens et al., 2010),
270 the soma included Kv1 and Kv3 voltage-dependent potassium currents and a sodium current.
271 To this, however, was added a g_{Kt} conductance based on the voltage-clamp findings above,
272 and a persistent sodium current (NaP). NaP and g_{Kt} were modelled either deterministically or
273 stochastically with a dynamic noise variance (see Materials and methods for details).

274 In the deterministic model, interspike intervals were of two types: long, almost
275 stationary pauses, and periods of subthreshold oscillation, of unstable and variable amplitude,
276 at a frequency of about 28 Hz (Figure 6a). In a three-dimensional subspace of the (8-
277 dimensional) phase space of the model, displaying the activation variable of g_{Kt} as x, the
278 membrane potential as y, and the sodium inactivation variable as z, some of the dynamical
279 structure underlying this behaviour can be seen (Figure 6b, Video 1). The subthreshold
280 oscillations correspond to variable numbers of circuits around an unstable-amplitude cycle in
281 one region of phase space, before the system escapes into the upstroke of a spike. Long
282 pauses correspond to a transition to another critically slow region of phase space where h, m,
283 and V remain at an almost fixed point, while Kv1 activation (n) slowly subsides, eventually
284 leading to an escape from this region, either directly into a spike, or into a period of

285 subthreshold oscillations. Thus, this set of conductances gives two dynamical mechanisms for
286 generating irregular interspike intervals: variable numbers of circuits of unstable amplitude
287 subthreshold oscillations, and long pauses in a slow region of phase space. The activation of
288 g_{Kt} is seen to vary considerably for different spikes (note the spread in values of m_{Kt} in the
289 afterhyperpolarization in Figure 6b).

290 Changing g_{Kt} and NaP conductances to a stochastic form somewhat obscures the
291 difference between the pauses and subthreshold oscillations, causing more irregular and
292 variable fluctuations in the subthreshold oscillations (Figure 6c). The subthreshold noise
293 amplitude is highly dependent on the stochastic g_{Kt}, since it is greatly reduced if g_{Kt} is
294 deterministic (Figure 6d). It is only slightly reduced if NaP is deterministic, but greatly
295 reduced if all voltage-gated sodium conductance is removed (Figure 6d, "TTX" - right hand
296 side). This implies that subthreshold fluctuations are dominated by g_{Kt}-driven stochastic
297 fluctuations which are strongly amplified by the voltage-gated sodium conductance – both are
298 required. The greater importance of g_{Kt} noise over NaP noise is largely due to its much
299 longer correlation time (10 ms versus 1 ms), which means that g_{Kt} noise is much less filtered
300 by the membrane time constant. Thus these strong subthreshold membrane potential
301 fluctuations appear to be actively-amplified channel noise, somewhat like noise-driven
302 subthreshold oscillations, as described in entorhinal stellate neurons (Dorval and White,
303 2005). This result suggests that, although the fit of the subthreshold membrane potential noise
304 variance by the "voltage-clamped" channel noise of NaP and g_{Kt} channels (Figure 3a, see
305 Materials and methods) appears to describe the onset of this noise reasonably well, the
306 numbers of channels are probably overestimated, as the powerful active amplification of
307 fluctuations is not taken into account.

308 The action of g_{Kt} in promoting irregular firing across the range of frequencies is
309 visualized in Figure 7, in which the firing frequency is plotted as a function of both stimulus
310 current and the amount of g_{Kt} conductance included in the model, with the surface colored to
311 indicate the CV(ISI). As the amount of g_{Kt} in the membrane is increased to 12 nS, a region
312 of structurally-stable variability is created for firing frequencies up to 20-30 Hz, above which
313 frequency the CV(ISI) subsides, as seen in recordings, in both deterministic (Figure 7a) and
314 stochastic (Figure 7b) forms of the model. In the deterministic form of the model, CV(ISI)
315 reaches values of ≈1, much higher than experimentally observed (red region of surface in
316 Figure 7a). However, the addition of noise dilutes the irregularity of this high-CV region to

317 ≈0.3 (Figure 7b), as seen experimentally. The stochastic model shows a much more linear
318 firing frequency-current (*f-I*) characteristic, as observed in actual recordings – i.e. the
319 dynamic noise linearizes the input-output relation of these neurons. The distribution of ISIs
320 produced by the stochastic model also resembles experimental distributions (Figure 6 – figure
321 supplement 1, panel a).

322

323 **Synchronization of irregular firing through gap-junctions in networks of model IS**
324 **neurons**

325 Irregular spiking could exert a far greater impact in the cortical network if it were
326 synchronized amongst IS neurons, which are connected with each other in a specific gap-
327 junction-coupled network (Galarreta et al., 2004). However, the mechanism of irregularity
328 proposed here depends on the intrinsic dynamics and noise sources within individual cells. It
329 seems possible that the impact of fluctuations generated within individual cells could be
330 diluted when cells are connected in an electrical network. Therefore, we simulated small
331 networks of symmetrically-coupled stochastic IS neurons. In a 5-cell network, firing becomes
332 highly synchronous as gap junction conductance was increased, as seen in the sharp central
333 peak of cross-correlation (Figure 7c). However, CV(ISI) was maintained at the same level as
334 for uncoupled cells, even with strong coupling and complete synchrony (Figure 7d). This
335 perhaps non-intuitive result implies that in effect, nonlinearly-amplified fluctuations are
336 cooperative amongst cells and are well-coupled by the current flow through gap junctions.

337

338 **Synchronization to oscillating input and the function of IS neurons**

339 The intrinsic irregularity of firing of IS neurons, which is distinctive amongst the cell types of
340 the cortical network, raises the question of what these neurons do, particularly in the context
341 of the regular firing which underlies organised oscillations in many frequency bands (Buszaki
342 and Draguhn, 2004). This particular type of IS neuron directly inhibits pyramidal neurons,
343 and it has been suggested that it might promote asynchronous firing and thereby resist
344 synchronous oscillations (Galarreta et al., 2008). In order to test how these cells integrate
345 periodic inputs, we examined their ability to synchronize their spikes to rhythmic oscillation
346 in a naturalistic stimulus consisting of several conductance components: a stationary, noisy
347 AMPA receptor-type excitatory conductance and an oscillating (10 Hz or 40 Hz) $GABA_A$

348 receptor-type shunting inhibitory conductance, combined with simultaneously adding or
349 subtracting g_{Kt} using dynamic-clamp (Figure 8a). Figure 8b shows an example of an
350 irregular cell subjected to an elevation of g_{Kt} (+3.57 nS g_{max0}). This depresses the synchrony
351 of spikes to the g_{GABA} rhythm (Figure 8b*ii*, *iii*) across the range of oscillation amplitudes
352 tested. Conversely, subtraction of g_{Kt} from another cell (Figure 8c) enhanced synchrony over
353 a wide range of oscillation amplitudes. These striking effects of g_{Kt} on synchrony to 10 Hz
354 inputs are not observed, however, for 40 Hz input (Figure 8d, summary statistics for the
355 whole set of cells at both frequencies are shown in Figure 8e). Thus modulation of
356 irregularity of IS neurons by the level of g_{Kt} (see Figures 5 and 6) appears to determine their
357 ability to synchronize to oscillatory inhibition, and the dynamics of g_{Kt} are such that it can
358 interact effectively with 10 Hz but not 40 Hz rhythms. Rejection of synchronization results
359 from the intrinsically irregular dymamics at lower frequencies, around 10 Hz, while
360 resonance with a noise-obscured subthreshold oscillation (whose frequency in the
361 deterministic model is 28 Hz) could contribute to the good synchronization at higher
362 frequencies. Thus the native g_{Kt} of IS cells allows them to resist synchrony to lower network
363 frequencies such as 10 Hz, while complying readily with higher, gamma frequency rhythms.
364 This could have the effect of destabilizing lower frequency network oscillations while
365 helping to stabilize higher-frequency rhythms, and help to determine the times of onset and
366 offset of organized gamma-frequency firing in the network.

367

368 **DISCUSSION**

369 Here we have used a combination of experiment and modelling to show that the voltage-
370 dependent gating and stochastic activation of fast-inactivating potassium and sodium
371 channels play major roles in generating the intrinsic irregularity of cortical irregularly-spiking
372 (IS) inhibitory interneurons. We also showed that at frequencies matching firing frequencies
373 where this irregularity is high (up to 20 Hz), these cells strongly reject synchronization to
374 naturalistic oscillating input. This finding is especially relevant considering that irregular-
375 spiking VIP interneurons fire at 10-15 Hz *in vivo* (whisking and non-whisking activities, Lee
376 et al., 2013).

377 IS cells have been hard to define functionally, because of the profusion of types of
378 inhibitory interneuron in the cortex, and because irregular-spiking behaviour may also arise
379 from fluctuations in synaptic input or membrane integrity during recordings. The

380 development of a genetically-modified mouse in which intrinsically IS cells are labelled with
381 GFP has allowed targeted study of a relatively homogeneous population of IS neurons
382 (Galarreta et al., 2004, 2008; Lopez-Bendito et al., 2004). Inducible *in vivo* genetic fate
383 mapping (Miyoshi and Fishell, 2010; Miyoshi et al., 2010) has been used to show that these
384 IS interneurons originate from the caudal ganglionic eminence relatively late in development
385 (E16), express 5HT3a receptors, VIP and calretinin, and form about 10% of CGE-derived
386 interneurons, which dominate the more superficial layers of cortex and comprise about 30%
387 of all cortical interneurons. Within upper layer 2, the lamina in which they are concentrated,
388 IS cells may make up a large proportion, perhaps 50% (Lopez-Bendito et al., 2004), of
389 interneurons. Though we know quite a lot about their functional synaptic connectivity, and its
390 regulation by CB1 receptors (Galarreta et al., 2004, 2008), the origin of the irregular spiking
391 behaviour itself has remained unknown.

392 Predictability of spike trains of irregular-spiking cortical neurons, has been examined
393 in a previous study (Englitz et al., 2008), which concluded that the variability is not a
394 consequence of low-dimensional, effectively deterministic processes. However, that study did
395 not examine the genetically-defined population of neurons studied here. In contrast, we found
396 that there was both significant recurrence and determinism, i.e. predictability, in sequences of
397 spike intervals, in about half of the cells examined (Figure 2). We propose that this
398 predictability is linked to the dynamics of a prominent low-threshold fast-inactivating
399 voltage-gated potassium conductance interacting with voltage-dependent sodium
400 conductance, including a persistent fraction, which enhances the activation of sodium
401 channels around AP threshold (Figures 3 and 4). Evidence for this was the sensitivity of
402 membrane fluctuations to TTX, the strong modulation of irregularity by injecting artificial
403 inactivating K^+ conductance, and the ability to reproduce this phenomenon in a biophysical
404 model (Figures 6 and 7).

405 We suggest that the fast-inactivating K^+ current that we found in these cells is likely
406 to be mediated by Kv4 potassium channel subunits, for several reasons. Not only does its fast
407 recovery from inactivation (≈40 ms) exclude the other main candidate, Kv1.4, but the current
408 was partially blocked by PhTX, and had weak voltage dependence for activation and
409 inactivation kinetics, which are known properties of Kv4-mediated currents. IS cells in this
410 same GFP mouse model have been shown to express high levels of Kv4.2 (kcnd2) mRNA,
411 higher than in a population of pyramidal cells and seven times higher than in a population of
412 fast-spiking interneurons (Sugino et al., 2006), but only very low levels of Kv1.4 (kcna4)

413 transcripts. The kinetics and voltage dependence of activation and inactivation also match
414 well those described for Kv4.1/4.2 in pyramidal neurons (Birnbaum et al., 2004). However,
415 further work will be needed to prove definitively the identity of these channels.

416 Interestingly, we found that GFP+ cells in dissociated primary cortical cultures also
417 showed robust intrinsic irregular firing (Figure 1e), and expressed transient K^+ and persistent
418 Na^+ currents (Figure 4 – figure supplement 3). This suggests that normal morphology and
419 circuit formation in development are not required for the irregularity. It is possible that the
420 relatively high mature input resistance of IS neurons (331 MΩ), compared to other types of
421 interneuron could directly lead to greater variability, since single-channel voltage noise
422 should be bigger. However, we found that when we injected an intense (2 nS) static shunting
423 conductance, reversing at -70 mV, near to the resting potential – effectively greatly reducing
424 input resistance, the action potential is reduced in amplitude, and afterhyperpolarizations and
425 interspike membrane potential fluctuations are strongly diminished, but irregularity is not
426 reduced (Figure 5 – figure supplement 1). Likewise, adding the artificial K^+ conductance,
427 which also decreases input resistance, caused increased, not decreased firing variability. This
428 indicates that irregularity is produced by a more complex dynamical mechanism, driven
429 partially by stochastic channel opening, but also dependent on the nonlinearity of the
430 transient K^+ current.

431 The model that we have implemented suggests two deterministic active mechanisms
432 for high spike time variability: long "pause" states, in which the dynamical state is
433 presumably trapped near the "ghost" of a fixed point, and unstable subthreshold oscillations.
434 Both these mechanisms exist over a fairly wide range of values of g_{Kt} conductance density
435 and stimulus level (Figure 7), but depend on the presence of g_{Kt}. The high irregularity and
436 variability of the purely deterministic form of the model is suggestive of deterministic chaos,
437 although a rigorous proof of chaos in the model would require for example proof of a positive
438 Lyapunov exponent, and is beyond the scope of this study. At the same time, however, it is
439 clear that significant dynamical noise must be involved to some extent in the irregularity, as a
440 result of the single-channel characteristics of the main voltage-dependent channels involved.
441 ISI distributions in IS neurons appear to be shaped by the single-channel current fluctuations
442 around the threshold (Figures 3 and 4), both of sodium channels including persistent ones,
443 and g_{Kt} channels. Adding noise in the model, which mimics the single-channel activity of
444 these channels around threshold, realistically obscures the regularity of the subthreshold
445 oscillation, and leads to ISI distributions very similar to those observed experimentally

446 (Figure 6 – figure supplement 1, panel a). While still clearly preserving the g_{Kt}.-induced
447 region of high-CV firing (Figure 7b), the addition of noise changes the unnaturally high
448 CV(ISI) of the deterministic model (≈1) to a value compatible with the experiments (≈0.3).
449 Thus, we believe that the interaction of both elements, the nonlinear deterministic Hodgkin-
450 Huxley equations and the single-channel dynamical noise is needed for an adequate
451 description of irregular spiking. Both the deterministic and stochastic components of the
452 model have measurable biophysical parameters.

453 Other, related dynamical models of irregular firing in neurons have been proposed.
454 For example, a bifurcation analysis (Golomb et al., 2007) of an FS cell model, incorporating
455 different levels of slowly-inactivating potassium current (I_d, probably corresponding to Kv1
456 channels) showed that higher levels of this current can produce "stuttering" behaviour
457 associated with subthreshold oscillations, as also seen experimentally in FS neurons (Tateno
458 et al., 2004). Dispersion of interspike intervals produced by variations in amplitude of
459 subthreshold oscillations of a much higher frequency (100-150 Hz) characterized in spinal
460 motoneurons has been termed "mixed-mode" oscillation (Manuel et al., 2009, Iglesias et al.,
461 2011). Noise-induced switching between a fixed point and a spiking limit cycle has been
462 shown to produce high irregularity in the Hodgkin-Huxley model (Rowat, 2007). Recently,
463 Stiefel et al. suggested that fast-activating K^+ currents could promote this kind of switching
464 behaviour in IS neurons, leading to high irregularity (Stiefel et al., 2013). Although the
465 mechanism that we propose here is both more specific and more complex, the basic necessity
466 for an interaction between noise and strong nonlinearity assisted by fast K^+ channels is
467 consistent with these studies. Interestingly, A-type potassium and NaP currents have also
468 been implicated in the generation of theta-frequency (5-10 Hz) membrane potential
469 oscillations in hippocampal interneurons (Morin et al., 2010, Skinner, 2012), possibly
470 through the dynamical mechanism of "critical slowing", in which the amplitude of noise-
471 driven fluctuations grows near a bifurcation. This may also be relevant in IS neuron
472 membrane potential fluctuations, and further studies of their sensitivity to noise near
473 threshold would be merited.

474 The active irregularity produced by coordinated activation of populations of voltage-
475 dependent channels and their activation-dependent single-channel noise, which we propose,
476 may have at least two important advantages. First, it is an energetically-favourable way to
477 generate high spike interval irregularity in individual cells, while minimizing unnecessary
478 membrane potential fluctuation, because fluctuations switch on sharply just below AP

threshold, and their active amplification makes them highly effective at controlling spike timing. Second, IS cells are linked to each other in a specific gap-junction-coupled network, and also inhibit each other through $GABA_A$ synapses (Galarreta et al., 2004, 2008). This would be expected to enhance the local synchrony of irregular firing (Gouwens et al., 2010), potentially greatly increasing their impact on network activity. The partly active, deterministic nature of irregularity and the subthreshold dynamics would help to coordinate the sources of irregularity in different cells, via current flow through gap junctions. Examining the synchronization of ensembles of stochastically-modelled IS neurons connected through gap junctions (Figure 7c, d), we found that even with high gap-junctional coupling and resultant complete synchrony of firing, irregularity is maintained just as high as in isolated neurons. This non-trivial result implies that the network of IS neurons can indeed fire with both high irregularity and precise synchrony.

Overall, these results suggest that coordinated irregular firing is important for the cortex. Synchronous oscillation, although it is a population activity that is relatively easily detected and studied, and which may provide a timing mechanism for processing, is also low-dimensional and limited in its capacity to represent information. Synchronous irregular firing may help to create diverse network firing patterns, useful in representation of information, and to find solutions to optimization problems in pattern recognition. It may also enhance STDP-based learning (Christodoulou and Cleanthous, 2011), and could be important in decision-making and generation of spontaneous choices. The coupled network of IS neurons could also control initiation and termination of periods of synchronous regular oscillations, consistent with the rejection of synchronization to low-frequency rhythms which we observed (Figure 8), which was enhanced by addition of artificial g_{Kt}.

In conclusion, we have provided evidence that, in addition to the direct effect of stochastic channel noise, IS neurons have a specific nonlinear deterministic mechanism that drives spike time irregularity. The mechanism depends on a nonlinear interaction of Kv4 potassium and sodium channels around threshold. This novel mechanism appears to allow this group of neurons to have a coordinated, and hence powerful, impact on concerted activity in the cortex.

509 **MATERIALS AND METHODS**

510 **Animals and tissue preparation**

511 A genetically-modified mouse line was used, in which GFP was linked to the promoter for
512 *Gad2* (Lopez-Bendito et al., 2004). At ages between P30 and P60, animals were sacrificed in
513 accordance with the UK Home Office regulations under the Animals (Scientific Procedures)
514 Act of 1986, and 300 μm sagittal slices of the neocortex were cut with a tissue slicer (Leica
515 VT1200S, Leica UK, Cambridge), using standard techniques described elsewhere (Morita et
516 al., 2008; Kim and Robinson, 2011). Slices were observed using an upright microscope
517 (Olympus BX51WI, XLUMPlanFI 20X/0.95W objective) with infrared illumination and an
518 oblique condenser, combined with epifluorescence to visualize GFP-expressing neurons.

519 Primary cultures of dissociated cortical *Gad2*-GFP neurons were obtained by methods
520 similar to those described by Schroeter et al. (2015). Extrahippocampal cortex was isolated at
521 E17 or P0, and cultured for 12-17 days in vitro. All protocols followed UK Home Office
522 regulations for care and use of animals.

523 **Solutions**

524 During recording, slices were superfused with a solution containing (mM): 125 NaCl, 25
525 $NaHCO_3$, 2.5 KCl, 1.25 NaH_2PO_4, 2 $CaCl_2$, 1 $MgCl_2$, 0.01 glycine, 25 D-glucose, maintained
526 at a pH of 7.4 by bubbling with 95% O_2, 5% CO_2 gas mixture. In most experiments, 10 μM
527 CNQX, 10 μM APV and 10 μM gabazine were added to silence background synaptic activity
528 in the slice. For whole-cell recordings, the following pipette filling solution was used (mM):
529 105 K gluconate, 30 KCl, 10 4-(2-hydroxyethyl)-1-piperazineethanesulfonic acid (HEPES), 4
530 ATP-Mg, 0.3 GTP-Na, 10 creatine phosphate-Na (adjusted to pH 7.3 with KOH, -10 mV
531 liquid junction potential (LJP)). In recordings with elevated calcium buffering (see text), the
532 concentration of K gluconate was reduced to 90 mM, and 10 mM 1,2-bis(o-
533 aminophenoxy)ethane-N,N,N',N'-tetraacetic acid (BAPTA)-Na was added. In the case of
534 whole-cell recordings of persistent sodium currents, the following intracellular solution was
535 used (mM): 90 Cs methanesulfonate, 30 CsCl, 10 BAPTA, 10 HEPES (adjusted to pH 7.3
536 with HCl, -12 mV LJP). For cell-attached recordings, the following pipette solution was used
537 (mM): 150 NaCl, 2.5 KCl, 12.5 tetraethylammonium (TEA) chloride, 2 $CaCl_2$, 1 $MgCl_2$, 10
538 HEPES. Potassium currents were measured with 300 nM TTX added to the bath solution.
539 Blockers were dissolved in a HEPES buffered aCSF and puff-applied through a glass pipette

540 of around 50 μm in tip diameter. Salts were obtained from Sigma-Aldrich (Dorset, UK), and
541 channel and receptor blockers from Tocris Bioscience (Bristol, UK), with the exception of
542 phrixotoxin, which was acquired from Abcam (Cambridge, UK). Recordings were carried at
543 30-33 ºC.

544 **Electrical recording**

545 Whole-cell recording in current-clamp and voltage-clamp modes, and cell-attached single-
546 channel recording were carried out using a Multiclamp 700B amplifier (Molecular Devices,
547 Sunnyvale, CA, USA), and Matlab (Mathworks, Natick, MA, USA) scripts calling NI-
548 DAQmx library functions (National Instruments, Austin, TX, USA) to acquire and generate
549 analog waveforms, using a National Instruments X-series DAQ interface. For current-clamp
550 and voltage-clamp, the built-in series resistance compensation and capacitance cancellation
551 circuitry of the Multiclamp were used. Pipettes (5-10 MΩ before sealing) were pulled from
552 borosilicate glass capillaries (GC150F-7.5, Harvard Apparatus, Kent, UK), and, for single-
553 channel recordings, coated with Sylgard (Dow Corning Europe, Belgium), and fire-polished.
554 Signals were filtered at 6 kHz (-3 dB, 4-pole Bessel) and sampled at 20 kHz with 16-bit
555 resolution. For conductance injection / dynamic-clamp (Destexhe and Bal, 2009) experiments,
556 a hard real-time SM2 system (Cambridge Conductance, Cambridge, UK) was used, with low-
557 latency AD and DA converters, and a digital signal processor (TMS C6713), running at a
558 sample / update rate of >50 kHz (<20 μs) (Robinson, 2008). Soma size (see Results) was
559 used to select putative IS cells in experiments where spiking pattern was not assessed, e.g.
560 cell-attached recordings.

561 **Statistics**

562 All measurements are given as mean ± standard error of the mean (SEM), unless otherwise
563 stated. To test for differences between two conditions, the two-sided Wilcoxon rank sum test
564 (Matlab Statistics Toolbox function `ranksum`), equivalent to the Mann-Whitney U test, was
565 used. n, the number of samples, and p, the probability of observing the two distributions
566 under the null hypothesis that they have equal medians, are given in all cases, and $p<0.05$ is
567 taken as the significance level.

568 **Spike analysis**

569 Spike times were determined as the times of positive-going threshold crossings of the
570 membrane potential at a threshold set at 10 mV below the peak of action potentials.

Variability of the phase of spikes during sinusoidal stimulation (Figure 8) was characterized by a phase order parameter, or synchrony of entrainment $S = \sqrt{\langle \cos^2(\phi) \rangle + \langle \sin^2(\phi) \rangle}$, which varied between 0 (phases distributed uniformly between 0 and 2π) and 1 (phases all identical). Spike times within the first 250 ms of each response were omitted, to exclude initial adaptation from the analysis. The cross-correlation function of firing between gap-junction-coupled model neurons was calculated by binning times of occurrence of spikes in one cell relative to those in another cell (Figure 7c). Instantaneous firing rate was obtained by dividing the number of spikes in each time bin (0.5 ms) by the total simulation period and by the time bin. Synchrony of spikes between coupled model neurons (Figure 7d) was characterized as the fraction of spikes in one cell which occur within ±10 ms of a spike in the other cell (obtained by integrating the cross-correlation function between -10 and +10 ms).

Time series analysis

Recurrence plot (RP) analysis (Eckmann et al., 1987) was carried out using the Cross Recurrence Plot (CRP) Matlab toolbox (Marwan et al., 2007). Briefly, let the time series of sequential interspike intervals be indexed as $\{x_{1-m+1}, x_{1-m+2}, \dots, x_1, x_2, \dots, x_N\}$. For each trial, the initial transient in the first 400 ms was excluded, slow within-trial nonstationarity (< 10% change in local average ISI) was removed by subtracting the least-square fit of the sequence to a second-order polynomial, and ISIs were normalized to zero mean, unit standard deviation. The state of the system at each interval *i* can be represented by a vector of length *m* of the immediately preceding intervals: $\vec{x}_i = [x_{i-m+1}, x_{i-m+2}, \dots, x_i]$. The time series is said to be embedded with dimension *m*. The elements in the RP matrix are determined as follows

$$\mathbf{R}_{i,j} = \begin{cases} 1 : \vec{x}_i \approx \vec{x}_j \\ 0 : \vec{x}_i \not\approx \vec{x}_j \end{cases}, \qquad i, j = 1, 2, \dots, N ,$$

where *N* is the number of sequential states, and $\vec{x}_i \approx \vec{x}_j$ means equality within a distance (or error) of ε. Points of value 1 are plotted as black dots, 0 as white. Recurrence (for a given ε) is defined as the fraction of points in the RP which are 1, while determinism is the proportion of recurrent points which lie within diagonal lines of slope one and length greater than one. To measure distance between embedding points, we used a Euclidean norm (Marwan et al., 2007), and ε was set at one standard deviation of the ISIs. Significance of both recurrence and determinism was measured by calculating the distribution of surrogate values obtained by randomly permuting one of the two time series in each cross-recurrence comparison, one

thousand times, and a *z*-test to estimate the probability *p* of obtaining the result by chance, with $p<0.05$ deemed significant.

Fitting of voltage-clamped g_{Kt} and dynamic conductance injection.

A Hodgkin-Huxley-type model with one activation variable (*m*) and one inactivation variable (*h*) was fitted to step responses in voltage-clamp, such that $I_{Kt} = g_{Kt}(V - E_K)$ $g_{Kt} = \bar{g}_{Kt}mh$. For dynamic conductance injection, three different parameter sets obtained from experiments were used, differing slightly in activation and inactivation kinetics, as follows.

Models 1 and 2:

$\frac{dm}{dt} = \alpha_m(1-m) - \beta_m m$ and $\frac{dh}{dt} = \alpha_h(1-h) - \beta_h h$, where

Model 1:

$$\alpha_m(V) = \frac{0.0187*(V+52.5)}{1-\exp\left((52.5-V)/1.96\right)} \quad , \qquad \beta_m(V) = 1.88 * \exp\left((80.62 - V)/74.36\right)$$

$$\alpha_h(V) = 0.0765 * \exp\left((61.63 - V)/9.16\right) \quad , \qquad \beta_h(V) = \frac{0.0514}{1+\exp\left((83.86-V)/1.03\right)}$$

Model 2:

$$\alpha_m(V) = \frac{0.0175*(V+73.2)}{1-\exp\left((73.2-V)/5.59\right)} \quad , \qquad \beta_m(V) = 1.47 * \exp\left((68.6 - V)/44.2\right)$$

$$\alpha_h(V) = 0.057 * \exp\left((51.34 - V)/29\right) \quad , \quad \beta_h(V) = \frac{0.054}{1+\exp\left((26.58-V)/23.72\right)} .$$

Model 3:

$\frac{dm}{dt} = \frac{m_\infty - m}{\tau_m}$ and $\frac{dh}{dt} = \frac{h_\infty - h}{\tau_h}$, with

$$m_\infty(V) = \frac{1}{1+\exp\left((-30-V)/10\right)} \quad , \qquad \tau_m(V) = 0.346\exp(-V/18.272) + 2.09$$

$$h_\infty(V) = \frac{1}{1+\exp\left(0.0878(V+55.1)\right)} \quad , \qquad \tau_h(V) = 2.1\exp(-V/21.2) + 4.627$$

All three models gave similar results, which are pooled together. To facilitate comparison across models and with a model-independent measure from experimental results, we characterise the amount of conductance measured in voltage-clamp, and injected with each model by the peak transient value reached at a potential of 0 mV, g_{max0}, rather than by $\bar{g}_{Kt}$.

623

624 **Fitting voltage-dependence of membrane potential noise**

625 The onset of TTX-dependent voltage noise with depolarization (Figure 3a) was fitted by
626 assuming that it was due only to non-inactivating (persistent) voltage-dependent sodium
627 channels and inactivating g_{Kt} channels, in a single passive cell compartment (i.e. without
628 considering the effect of changes in the membrane potential on channel gating, including
629 active amplification by the large Na conductance in the cell), whose passive conductance is G,
630 and membrane time constant is τ_{cell}. Let $\tau_m = 1/(\alpha_m + \beta_m)$ and $m_\infty = \alpha_m/(\alpha_m + \beta_m)$.
631 Then by calculating the Lorentzian components of the single-channel noise expected from the
632 Hodgkin-Huxley model, filtering with the membrane time constant and integrating over all
633 frequencies (Schneidman et al., 1998), we obtain the following distribution of membrane
634 potential variance, for NaP channels:

$$\sigma_V^2 = \frac{N^2 i^2 m_\infty^3}{G^2}\left[3m_\infty^2(1-m_\infty)\frac{\tau_m}{\tau_m+\tau_{cell}} + 3m_\infty(1-m_\infty)^2\frac{\tau_m/2}{\tau_m/2+\tau_{cell}} + (1-m_\infty)^3\frac{\tau_m/3}{\tau_m/3+\tau_{cell}}\right]$$

635 N is the number of channels and i, the single channel current is given by $(V - E_{Na})$, where γ
636 is the single-channel conductance. For g_{Kt} channels, $i = \gamma(V - E_K)$ and

$$\sigma_V^2 = \frac{N^2 i^2 m_{Kt,\infty} r_{Kt,\infty}}{G^2}\left[h_{Kt,\infty}\left(1-m_{Kt,\infty}\right)\frac{\tau_{mKt}}{\tau_{mKt}+\tau_{RC}} + m_{Kt,\infty}\left(1-h_{Kt,\infty}\right)\frac{\tau_{hKt}}{\tau_h+\tau_{RC}} + \left(1-m_{Kt,\infty}\right)\left(1-h_{Kt,\infty}\right)\frac{\tau_1}{\tau_1+\tau_{RC}}\right]$$

637 where $\tau_1 = \tau_{mKt}\tau_{hKt}/(\tau_{mKt} + \tau_{hKt})$. The total membrane noise variance was taken as the
638 sum of these two components.

639

640 **Model of irregular spiking**

641 A reduced conductance-based model of IS neurons was implemented in Java (called from
642 Matlab, see source code in irregmodelcode.zip), based on a standard model of fast-spiking
643 inhibitory interneurons (Erisir et al., 1999; Gouwens et al., 2010), to which was added a
644 second compartment modelling dendritic membrane, a g_{Kt} potassium conductance whose

kinetics was obtained from fits to the voltage clamp data shown in Figure 4, and noise sources representing the effects of persistent sodium and g_{Kt} channel openings. A somatic compartment, of capacitance C = 8.04 pF and passive leak conductance g_L = 4.1 nS, was connected with an intracellular resistance R_i of 2 GΩ to a passive compartment representing remote dendritic membrane, which had a capacitance C_D of 80 pF and a leak conductance g_D of 0.5 nS. Transient sodium (Na) and persistent sodium (NaP), Kv1 (K1), Kv3 and g_{Kt} type potassium and static leak (L) conductances were inserted at the soma. The system of differential equations describing the model was as follows. The somatic voltage V was determined by a Langevin equation containing noise terms X for NaP and g_{Kt} channel fluctuations:

$$C\frac{dV}{dt} = (\bar{g}_{Na}m^3h + \bar{g}_{NaP}m^3)(E_{Na} - V) + (\bar{g}_{K1}n^4 + \bar{g}_{K3}p^2 + \bar{g}_{Kt}m_{Kt}h_{Kt})(E_K - V) + g_L(E_L - V) + X_{NaP} + X_{Kt} + I_{stim}$$

The voltage of the passive dendritic compartment was determined by:

$$C_D\frac{dV_D}{dt} = (V - V_D)/R_i + g_D(E_L - V_D)$$

The kinetics of the gating variables of voltage-dependent channels were determined as follows (units of mV for voltage, ms^{-1} for rates):

$\frac{dx}{dt} = \alpha_x(V)(1-x) - \beta_x(V)x$, for $x \in \{m, h, n, p\}$, where

$\alpha_m(V) = (3020 - 40V)/(\exp((-75.5 + V)/-13.5) - 1)$, $\beta_m = 1.2262/\exp(V/42.248)$,

$\alpha_h(V) = 0.0035/\exp(V/24.186)$, $\beta_h(V) = -(0.8712 + 0.017V)/(\exp((51.25 + V)/-5.2) - 1)$,

$\alpha_n(V) = -(0.616 + 0.014V)/(\exp((44 + V)/-2.3) - 1)$, $\beta_n(V) = 0.0043/\exp((44 + V)/34)$,

$\alpha_p(V) = (95 - V)/(\exp((-95 + V)/-11.8) - 1)$, $\beta_p(V) = 0.025/\exp(V/22.222)$

And $\frac{dm_{Kt}}{dt} = \frac{m_{Kt,\infty} - m_{Kt}}{\tau_{mKt}}$ and $\frac{dh_{Kt}}{dt} = \frac{h_{Kt,\infty} - h_{Kt}}{\tau_{hKt}}$, with

$m_{Kt,\infty}(V) = \frac{1}{1+\exp((-30-V)/10)}$, $\tau_{mKt}(V) = 0.346\exp(-V/18.272) + 2.09$

$$h_{Kt,\infty}(V) = \frac{1}{1+\exp(0.0878(V+55.1))}, \qquad \tau_{hKt}(V) = 2.1\exp(-V/21.2) + 4.627$$

$\bar{g}_{Na}$=900 nS, $\bar{g}_{K1}$=1.8 nS, $\bar{g}_{Na}$=1800 nS, g_L=4.1 nS, E_L=-70 mV, E_K=-90 mV, E_{Na}=60 mV. Values of $\bar{g}_{Na}$, $\bar{g}_{K1}$ and $\bar{g}_{K3}$ are unchanged from those used for fast-spiking interneurons in Erisir et al., 1999 and Gouwens et al., 2010, while g_L was adjusted to give a resting input resistance similar to those measured in IS neurons. $\bar{g}_{Kt}$ was set to 7 nS or varied as described in the text (deterministic case), or 700 × 10 pS channels, or varied as described (stochastic case). $\bar{g}_{NaP}$ was set to 10 nS (deterministic) or 500 × 20 pS channels (stochastic case, see below).

The single persistent sodium channel current was given by $i = \gamma(E_{Na} - V)$ where i is the single sodium channel current and γ is the single channel conductance, set to 20 pS. Macroscopic persistent Na current was given by $I_{NaP} = \bar{I}_{NaP} + X$, where the deterministic mean current term was given by $\bar{I}_{NaP} = Nim^3$ in which N is the number of persistent sodium channels (0 for the deterministic model, see text), and the noise term X was updated at each time step by the exact update formula for an Ornstein-Uhlenbeck process (Gillespie, 1996):

$$X_{t+\Delta t} = X_t \exp(-\Delta t/\tau_o) + \xi\sqrt{\sigma_{NaP}^2[1-\exp(-2\Delta t/\tau_o)]}$$

where Δt is the time step of integration, τ_o is the mean opening burst time of persistent Na channel openings, set at 1 ms, and ξ is a normally-distributed (mean 0, variance 1) random number. The variance of X changed dynamically, according to the mean level of persistent sodium current, as:

$$\sigma_{NaP}^2 = i\bar{I}_{NaP} - \bar{I}_{NaP}^2 / N .$$

g_{Kt} noise was modelled similarly, a single channel conductance of 10 pS, and a mean opening burst time of 10 ms, estimated from recordings.

A fourth-order Runge-Kutta method (Press et al., 2002) was used to integrate deterministic variables, with a time step of 5 or 1 μs. The value of the noise term was updated in parallel, as described above, and interpolated linearly at the midpoint of full Runge-Kutta steps. This gave identical results to an Euler-Maruyama method (Kloeden and Platen, 1992), but with improved stability and efficiency.

ACKNOWLEDGMENT

The authors would like to thank Paul Charlesworth (University of Cambridge) for providing primary cultures of dissociated cortical neurons.

REFERENCES

Alonso, A. and Klink, R. (1993) Differential electroresponsiveness of stellate and pyramidal-like cells of medial entorhinal cortex layer II. J. Neurophysiol. *70*, 128-143.

Alonso, G., and Widmer, H. (1997). Clustering of Kv4.2 potassium channels in postsynaptic membrane of rat supraoptic neurons: an ultrastructural study. Neuroscience *77*, 617-621.

Amarillo, Y., De Santiago-Castillo, J. a, Dougherty, K., Maffie, J., Kwon, E., Covarrubias, M., and Rudy, B. (2008). Ternary Kv4.2 channels recapitulate voltage-dependent inactivation kinetics of A-type K+ channels in cerebellar granule neurons. J. Physiol. *586*, 2093–2106.

Ascoli, G.A., Alonso-Nanclares, L., Anderson, S.A. *et al.* (2008). Petilla terminology: nomenclature of features of GABAergic interneurons of the cerebral cortex. Nat. Rev. Neurosci. *9*, 557-568.

Bean, B.P. (2007). The action potential in mammalian central neurons. Nat. Rev. Neurosci. *8*, 451-465.

Birnbaum, S.G., Varga, A.W., Yuan, L.L., Anderson, A.E., Sweatt, J.D., and Schrader, L.A. (2004). Structure and function of Kv4-family transient potassium channels. Physiol Rev *84*, 803-833.

Buszaki, G., and Draguhn, A. (2004). Neuronal oscillations in cortical networks. Science *304*, 1926-1929.

Buszsaki, G. (2006). Rhythms of the Brain (New York: Oxford University Press).

Cardin, J.A., Carlen, M., Meletis, K., Knoblich, U., Zhang, F., Deisseroth, K., Tsai, L.H., and Moore, C.I. (2009). Driving fast-spiking cells induces gamma rhythm and controls sensory responses. Nature *459*, 663-667.

Cauli, B., Audinat, E., Lambolez, B., Angulo, M.C., Ropert, N., Tsuzuki, K., Hestrin, S., and Rossier, J. (1997). Molecular and physiological diversity of cortical nonpyramidal cells. J. Neurosci. *17*, 3894-3906.

Christodoulou, C., and Cleanthous, A. (2011). Does High Firing Irregularity Enhance Learning? Neural Comput. *23*, 656-663.

Cooper, E. and Shrier, A. (1989) Inactivation of A currents and A channels on rat nodose neurons in culture. J. Gen. Physiol. *94*, 881-910.

Destexhe, A., and Bal, T., eds. (2009). Dynamic-Clamp: From Principles to Applications (Springer).

Destexhe, A., Rudolph, M., Fellous, J.M., and Sejnowski, T.J. (2001). Fluctuating synaptic conductances recreate in vivo-like activity in neocortical neurons. Neuroscience *107*, 13-24.

Dorval, A.D., and White, J.A. (2005). Channel noise is essential for perithreshold oscillations in entorhinal stellate neurons. J. Neurosci. *25*, 10025-10028.

Durstewitz, D., and Gabriel, T. (2007). Dynamical basis of irregular spiking in NMDA-driven prefrontal cortex neurons. Cereb. Cortex *17*, 894-908.

Eckmann, J.-P., Kamphorst, S.O., and Ruelle, D. (1987). Recurrence plots of dynamical systems. Europhysics Lett. *5*, 973-977.

Englitz, B., Stiefel, K.M., and Sejnowski, T.J. (2008). Irregular firing of isolated cortical interneurons in vitro driven by intrinsic stochastic mechanisms. Neural Comput. *20*, 44-64.

Erisir, A., Lau, D., Rudy, B., and Leonard, C.S. (1999). Function of specific K(+) channels in sustained high-frequency firing of fast-spiking neocortical interneurons. J. Neurophysiol. *82*, 2476-2489.

Fan, Y.S., and Chay, T.R. (1994). Generation of periodic and chaotic bursting in an excitable cell model. Biol. Cybernetics *71*, 417-431.

Fanselow, E.E., Richardson, K.A., and Connors, B.W. (2008). Selective, state-dependent activation of somatostatin-expressing inhibitory interneurons in mouse neocortex. J. Neurophysiol. *100*, 2640-2652.

FitzHugh, R. (1961). Impulses and physiological states in theoretical models of nerve membrane. Biophys. J. *1*, 445-466.

Galarreta, M., Erdelyi, F., Szabo, G., and Hestrin, S. (2004). Electrical coupling among irregular-spiking GABAergic interneurons expressing cannabinoid receptors. J. Neurosci. *24*, 9770-9778.

Galarreta, M., Erdelyi, F., Szabo, G., and Hestrin, S. (2008). Cannabinoid sensitivity and synaptic properties of 2 GABAergic networks in the neocortex. Cereb. Cortex *18*, 2296-2305.

Gillespie, D.T. (1996). Exact numerical simulation of the Ornstein-Uhlenbeck process and its integral. Phys. Rev. E 54, 2084-2091.

Golomb, D., Donner, K., Shacham, L., Shlosberg, D., Amitai, Y., and Hansel, D. (2007). Mechanisms of firing patterns in fast-spiking cortical interneurons. PLoS Comput. Biol. *3*, e156.

Gouwens, N., Zeberg, H., Tsumoto, K., Tateno, T., Aihara, K., and Robinson, H.P.C. (2010). Synchronization of firing in cortical fast-spiking interneurons at gamma frequencies: a phase-resetting analysis. PLoS Comput. Biol. *6*, e1000951.

Grace, A.A., and Bunney, B.S. (1984). The control of firing pattern in nigral dopamine neurons: single spike firing. J. Neurosci. *4*, 2866-2876.

Hasenstaub, A., Shu, Y., Haider, B., Kraushaar, U., Duque, A., and McCormick, D.A. (2005). Inhibitory postsynaptic potentials carry synchronized frequency information in active cortical networks. Neuron *47*, 423-435.

Hindmarsh, J.L., and Rose, R.M. (1984). A model of neuronal bursting using three coupled first order differential equations. Proc. Roy. Soc. Lond. B *221*, 87-102.

Hodgkin, A.L., and Huxley, A.F. (1952). A quantitative description of membrane current and its application to conduction and excitation in nerve. J. Physiol. *117*, 500-544.

Holmqvist, M.H., Cao, J., Hernandez-Pineda, R., Jacobson, M.D., Carroll, K.I., Sung, M.A., Betty, M. et al. (2002) Elimination of fast inactivation in Kv4 A-type potassium channels by an auxiliary subunit domain. Proc. Natl. Acad. Sci. USA *99*, 1035–1040.

Iglesias, C., Meunier, C., Manuel, M., Timofeeva, Y., Delestrée, N. and Zytnicki, D.. (2011) Mixed mode oscillations in mouse spinal motoneurons arise from a low excitability state. J. Neurosci. *31*, 5829-5840.

Jinno, S., Jeromin, A., and Kosaka, T. (2005). Postsynaptic and extrasynaptic localization of Kv4.2 channels in the mouse hippocampal region, with special reference to targeted clustering at gabaergic synapses. Neuroscience *134*, 483-494.

Kantz, H., and Schreiber, T. (1997). Nonlinear time series analysis (Cambridge: Cambridge University Press).

Kim, N.-K. and H.P.C. Robinson (2011) Effects of divalent cations on slow unblock of native NMDA receptors in mouse neocortical pyramidal neurons. Eur J Neurosci, 34: 199-212.

Kiss, T. (2008). Persistent Na-channels: origin and function. A review. Acta Biol. Hung. *59 Suppl*, 1-12.

Kloeden, P.E., and Platen, E. (1992). Numerical Solution of Stochastic Differential Equations (Springer).

Lee, S., Hjerling-Leffler, J., Zagha, E., Fishell, G., and Rudy, B. (2010). The largest group of superficial neocortical GABAergic interneurons expresses ionotropic serotonin receptors. J. Neurosci. *30*, 16796-16808.

Lee, S., Kruglikov, I., Huang, Z.J., Fishell, G., and Rudy, B. (2013). A disinhibitory circuit mediates motor integration in the somatosensory cortex. Nat. Neurosci. *16*, 1662–1670.

Lopez-Bendito, G., Sturgess, K., Erdelyi, F., Szabo, G., Molnar, Z., and Paulsen, O. (2004). Preferential origin and layer destination of GAD65-GFP cortical interneurons. Cereb. Cortex *14*, 1122-1133.

Maffie, J.K., Dvoretskova, E., Bougis, P.E., Martin-Eauclaire, M.-F., and Rudy, B. (2013). Dipeptidyl-peptidase-like-proteins confer high sensitivity to the scorpion toxin AmmTX3 to Kv4-mediated A-type K+ channels. J. Physiol. *591*, 2419–2427.

Manuel, M., Iglesias, C., Donnet, M., Leroy, F., Heckman, C.J., and Zytnicki, D. (2009). Fast kinetics, high-frequency oscillations, and subprimary firing range in adult mouse spinal motoneurons. J. Neurosci. *29*, 11246-11256.

Marwan, N., Romano, M.C., Thiel, M., and Kurths, J. (2007). Recurrence plots for the analysis of complex systems. Phys. Reports *438*, 237-329.

Miyoshi, G., and Fishell, G. (2010). GABAergic interneuron lineages selectively sort into specific cortical layers during early postnatal development. Cereb. Cortex *21*, 845-852.

Miyoshi, G., Hjerling-Leffler, J., Karayannis, T., Sousa, V.H., Butt, S.J., Battiste, J., Johnson, J.E., Machold, R.P., and Fishell, G. (2010). Genetic fate mapping reveals that the caudal ganglionic eminence produces a large and diverse population of superficial cortical interneurons. J. Neurosci. *30*, 1582-1594.

Morin, F., Haufler, D., Skinner, F.M., and Lacaille, J-C. (2010) Characterization of voltage-gated K^+ currents contributing to subthreshold membrane potential oscillations in hippocampal CA1 interneurons. J. Neurophysiol. *103*, 3472-3489.

Morita, K., Kalra, R., Aihara, K., and Robinson, H.P.C. (2008). Recurrent synaptic input and the timing of gamma-frequency-modulated firing of pyramidal cells during neocortical "UP" states. J. Neurosci. *28*, 1871-1881.

Pikovsky, A., Rosenblum, M., and Kurths, J. (2001). Synchronization: a universal concept in nonlinear sciences (Cambridge: Cambridge University Press).

Press, W.H., Teukolsky, S.A., Vetterling, W.T., and Flannery, B.P. (2002). Numerical Recipes in C++: The Art of Scientific Computing (Cambridge University Press).

Ribrault, C., Sekimoto, K., and Triller, A. (2011). From the stochasticity of molecular processes to the variability of synaptic transmission. Nat. Rev. Neurosci. *12*, 375-387.

Robinson, H.P.C. (2008). A scriptable DSP-based system for dynamic conductance injection. J. Neurosci. Meth. *169*, 271-281.

Robinson, H.P.C., and Kawai, N. (1993). Injection of digitally synthesized synaptic conductance transients to measure the integrative properties of neurons. J. Neurosci. Meth. *49*, 157-165.

Rowat, P. (2007). Interspike interval statistics in the stochastic Hodgkin-Huxley model: coexistence of gamma frequency bursts and highly irregular firing. Neural Comput. *19*, 1215-1250.

Schneidman, E., Freedman, B., and Segev, I. (1998). Ion channel stochasticity may be critical in determining the reliability and precision of spike timing. Neural Comput. 10, 1679-1703.

Schroeter, M.S., Charlesworth, P., Kitzbichler, M.G., Paulsen, O., and Bullmore, E.T. (2015). Emergence of rich-club topology and coordinated dynamics in development of hippocampal functional networks in vitro. J Neurosci *35*, 5459–5470.

Sharp, A.A., O'Neil, M.B., Abbott, L.F., and Marder, E. (1993). Dynamic clamp: computer-generated conductances in real neurons. J. Neurophysiol. *69*, 992-995.

Sigworth, F.J., and Neher, E. (1980). Single Na+ channel currents observed in cultured rat muscle cells. Nature *287*, 447-449.

Skinner, F.K. (2012) Cellular-based modeling of oscillatory dynamics in brain networks. Curr. Opin. Neurobiol. *22*, 660-669.

Sprott, J. (2003). Chaos and Time-Series Analysis (New York: Oxford University Press).

Stiefel, K.M., Englitz, B., and Sejnowski, T.J. (2013). Origin of intrinsic irregular firing in cortical interneurons. Proc. Natl. Acad. Sci. USA *110*, 7886-7891.

Sugino, K., Hempel, C.M., Miller, M.N., Hattox, A.M., Shapiro, P., Wu, C., Huang, Z.J., and Nelson, S.B. (2006). Molecular taxonomy of major neuronal classes in the adult mouse forebrain. Nat. Neurosci. *9*, 99-107.

Tateno, T., Harsch, A., and Robinson, H.P. (2004). Threshold firing frequency-current relationships of neurons in rat somatosensory cortex: type 1 and type 2 dynamics. J. Neurophysiol. *92*, 2283-2294.

Vierling-Claassen, D., Cardin, J.A., Moore, C.I., and Jones, S.R. (2010). Computational modeling of distinct neocortical oscillations driven by cell-type selective optogenetic drive: separable resonant circuits controlled by low-threshold spiking and fast-spiking interneurons. Front. Hum. Neurosci. *4*, 198.

Wickenden, A.D., Jegla, T.J., Kaprielian, R., and Backx, P.H. (1999). Regional contributions of *Kv1.4*, *Kv4.2*, and *Kv4.3* to transient outward K^+ current in rat ventricle. Am. J. Physiol. *276*, H1599-H1607.

White, J.A., Klink, R., Alonso, A., and Kay, A.R. (1998). Noise from voltage-gated ion channels may influence neuronal dynamics in the entorhinal cortex. J. Neurophysiol. *80*, 262-269.

FIGURE LEGENDS

Figure 1. Irregular-spiking in a population of cortical inhibitory interneurons. (**a**) Distribution of *Gad2*-GFP mouse neurons in the somatosensory cortex (top). Below is the detailed morphology of a typical irregular-spiking interneuron which was filled with neurobiotin. White arrow indicates the axon initial segment. Irregular-spiking *Gad2*-GFP interneurons were consistently found in superficial layers and displayed noticeably bigger somata. Stacked confocal images of cells in a 300 µm thick slice, scale bar 150 µm and 50 µm respectively. (**b**), (**i**) Irregular spiking in response to a constant 120 pA current step. Resting potential was -68 mV. After an initial fast spike doublet, firing settles into an irregular pattern of spikes, separated by noisy fluctuations of membrane potential. (**ii**) Raster plot of spike times in 30 successive responses to the same current step, separated by 10 s intervals. Spike train corresponding to (bi) is indicated by an arrow at left. (**c**) Close-up view of the interspike membrane potential fluctuations in three consecutive trials from the ensemble shown in (bii). Spikes have been truncated. (**d**), (**i**) Higher frequency firing in another cell, excited by a 220 pA constant current stimulus. (**ii**) The distribution of 2,730 interspike intervals (ISIs) in one cell, fitted to a gamma distribution: $f(t) = \frac{1}{\Gamma(n)\tau}\left(\frac{t-t_r}{\tau}\right)^{n-1}\exp\left(\frac{t_r-t}{\tau}\right), \quad t > t_r$ where n is 2.29, τ is 20.7 ms, and refractory period t_r is 35.05 ms. CV(ISI) = 0.38, mean firing frequency is 13.6 Hz. **(e)**, *Gad2*-GFP cortical interneurons display the same irregular-spiking pattern in primary culture (12-16 DIV; n=10). Irregularity increased with development, and was observable even at higher firing frequencies (15-20 Hz) as in cortical slices. (**f**) Patch-clamp recording of a GFP+ neuron in culture. Scale bar 50 µm.

Figure 2. Predictability and nonlinearity of interspike interval sequences. **(a)** Examples of two contrasting ISI return maps extracted from a regular-spiking cell (blue, mean frequency 9.67 Hz, CVISI = 0.075) and an irregular-spiking cell (red, mean frequency 9.65 Hz, CVISI =

899 0.207). (**b**) Segments of corresponding spike trains. (**c**) Principle of recurrence analysis.
900 Dynamical state of the process is represented by vectors of consecutive ISIs, or embedding
901 points. In this example, point $\mathbf{A_j}$ in a 3-dimensional embedding of an interspike interval
902 sequence A (whose coordinates are ISIs *j*-2, *j*-1 and *j*) is similar to point $\mathbf{B_k}$ in interspike
903 interval series B (top), because their distance is less than a threshold ε (bottom). (**d**) Selection
904 of stationary sequences of stimulus trials for recurrence analysis. The mean ISI in each trial
905 lasting 8 s, repeated at 25 s intervals, is plotted with its standard deviation (filled circles and
906 error bars), and the standard error of the mean (filled squares). Sections of the time series
907 were accepted as sufficiently stationary if the average trial-to-trial change in mean ISI was
908 less than half the average standard error of the mean (e.g. region shown in dashed gray
909 rectangle). (**e**) Example cross-recurrence plot between two consecutive stimulus trials, A and
910 B, embedding dimension m = 4, ε = one standard deviation of the ISIs. Position (i,j) is
911 colored according to the Euclidean distance between the length-4 ISI sequences at position *i*
912 in *A* and *j* in *B*. Thus blue points reflect recurrence of very similar patterns. (**f**) Four examples
913 of repeated patterns or "motifs" of ISIs in sequence B corresponding to the patterns at
914 positions (i) – (iv) in sequence A, as indicated in (e). See Figure 2 – figure supplement 1 and
915 Figure 2 – source data 2 for recurrence plot quantification.

916 **Figure 3.** Voltage-gated sodium channel activation is required for noisy subthreshold voltage
917 fluctuations. (**a**) The amplitude of subthreshold fluctuations (see example waveform in inset)
918 rises sharply above a threshold membrane potential (≈ -50 mV). Measurements for 23 cells
919 indicated by different symbols. The curve shows a fit to a model of combined NaP (1950
920 channels) and g_{Kt} (180 channels) single channel noise, see Materials and methods for details).
921 Inset: three example traces for one cell during step current stimulation of 60, 90 and 100 pA,
922 showing the onset of membrane potential noise. (**b**) Fluctuations are blocked by applying
923 tetrodotoxin (TTX, 100 nM). Membrane potential traces in another IS cell with and without
924 perfusion of TTX, in response to the same current step, which is subthreshold in the steady-
925 state after an initial doublet (top). Corresponding amplitude histogram of the membrane
926 potential (bottom). (**c**) Membrane current in a cell-attached patch in response to repeated
927 depolarizing steps, from rest-20 mV to rest+40 mV, as indicated. RP = resting membrane
928 potential. Sodium channel openings are both transient, within 10 ms of the depolarization,
929 and persistent, occurring late in the depolarization. (**d**) Transient and persistent openings at
930 higher time resolution. (**e**) Whole-cell recordings confirming the presence of a TTX-sensitive,
931 non-inactivating inward current at the firing threshold potential range (-55 mV). A slowly

932 depolarising ramp (20 mV/s, from -80 mV to -10 mV, -70 mV holding potential) was applied
933 in the presence of TEA (2 mM), 4-AP (2 mM) and Cd^{+2} (200 μM) in order to eliminate K^+
934 and Ca^{+2} currents, with TTX (500 nM) added during the trial shown in red.

935 **Figure 4.** IS neurons express a fast transient outward current with similar kinetics of Kv4. (**a**)
936 Whole-cell currents in response to a family of voltage steps from -80 to 0 mV in 5 mV steps.
937 (**b**) A-type current separated from other outward current components. The remaining step-
938 evoked current following a pre-pulse (-30 mV, 200 ms) capable of inactivating A-type
939 current was subtracted from total current. Voltage steps from -50 to +40 in 10 mV steps.
940 Recordings were carried in the presence of 5 mM TEA in order to block slowly activating K^+
941 currents. (**c**) Voltage-dependencies of steady-state activation and inactivation. (**d**) Activation
942 (red) and inactivation (blue) time constants of dissected A-type current (top) and recovery of
943 inactivation time constant (bottom). (**e**) The fast inactivating outward current found in these
944 cells was sensitive to the A-type current blocker 4-AP (7mM) and the Kv4-specific blocker
945 phrixotoxin (PhTX, 5 μM). Top panels: total currents in control, drug application, and
946 washout, as indicated. Lower panel: PhTX block of transient outward current fraction,
947 separated as in (b) **(f)** Average of 537 aligned APs following ISIs lasting longer than 100 ms
948 shows a small prespike dip or inflexion, attributed to the activation of the transient K^+ current.
949 **(g)**, (**i**) Isolated transient outward current with a single exponential fitted to the decay phase (τ
950 = 13.05 ms). (**ii**) Example current from a cluster of transient K^+ channels in a cell-attached
951 patch (step from RP-30 mV to RP+50 mV at the time indicated by arrow, outward current
952 plotted upwards), fitted with the same exponential time constant as in (i). (**h**) Dependence of
953 patch current on the potential of a 500 ms prepulse before a step from RP-30 to RP+50 mV,
954 showing that it inactivates over the range RP+10 mV to RP+40 mV.

955 **Figure 5.** Injection of synthetic g_{Kt} modulates spiking irregularity. (**a**) Positive and negative
956 g_{Kt} injection in the same cell at the same frequency range (8-10 Hz). While -8.7 nS injection
957 (g_{max0}, See Materials and methods) caused a reduction in the AHP amplitude and regularised
958 the firing pattern, injecting +8.7 nS created more evident noisy plateaus before some APs,
959 resulting in more irregular firing. Red bottom trace shows the current passed during the
960 positive g_{Kt} conductance injection (outward, hyperpolarizing current plotted downwards). **(b)**
961 Effect of g_{Kt} on spiking irregularity in another cell, showing its consistency in different firing
962 frequencies. **(c)** Close-up of the membrane potential trajectories from (a), $+g_{Kt}$ (red)
963 superimposed on control (black), showing extended and increased noisy subthreshold

964 fluctuations produced by the g_{Kt} conductance. **(d)** Potassium currents during a family of step
965 depolarizations from -80 mV to -60, -50, … +10 mV. Subtraction of 3.92 nS of the fast-
966 inactivating Kv current by dynamic-clamp largely cancels the transient component, leaving a
967 residual, non-inactivating delayed rectifier current. **(e)** Relative changes in CV(ISI) at 10 Hz
968 firing frequency induced by addition or subtraction of g_{Kt} conductance. Data from 42 cells:
969 points are individual measurements, with some cells measured at two or more different
970 conductance levels. Wilcoxon non parametric test, $p<9.8 \times 10^{-16}$ for positive g_{Kt}, and $p<1.6 \times$
971 10^{-8} for negative g_{Kt}. **(f)** Relationship between relative change in CV(ISI) at 10 Hz firing
972 frequency, and injected g_{Kt} conductance. Linear regression fit is superimposed. Pearson's
973 correlation $r = 0.59$, $p< 2.66 \times 10^{-12}$.

974 **Figure 6**. Irregular firing in a simple biophysically-based model. (**a**) Two-compartment
975 model with Nav, Kv1, Kv3 and g_{Kt}-type conductances shows complex spike timing, as a
976 result of unstable subthreshold oscillations and trapping in a nearly-fixed state. $\bar{g}_{Kt}$ = 7 nS,
977 stimulus current, 100 pA. For other parameters, see Materials and methods. (**b**) Unstable
978 subthreshold oscillations and a fixed-point "ghost" seen in the phase trajectory of the model
979 with zero noise in the (m_{Kt}, h_{Na}, V) subspace (101 pA, 7 nS $\bar{g}_{Kt}$). (**c**) Adding noisy non-
980 inactivating (persistent) sodium channel current (equivalent to 500 channels) and noisy g_{Kt}
981 current (equivalent to 7 nS or 700 channels) masks subthreshold oscillations, but preserves
982 high spike irregularity. Stimulus current 90 pA. (**d**) g_{Kt} channel noise is strongly amplified by
983 voltage-dependent sodium conductance. Subthreshold membrane potential noise for a
984 stimulus current of 72 pA, with 7 nS $\bar{g}_{Kt}$ and 10 nS $\bar{g}_{NaP}$, either stochastic or deterministic,
985 and for the case in which all sodium current is blocked ("TTX"), and stimulus current of 90
986 pA, to polarize the membrane to the same range of membrane potential as without sodium
987 current.

988 **Figure 7.** g_{Kt} enhances irregularity in deterministic and stochastic biophysical models. (**a**)
989 Surface showing the dependence of firing frequency on the total g_{Kt} and stimulus current
990 level, colored according to the CV(ISI) of firing. Regions of low CV(ISI) correspond to
991 periodic firing, while regions of high variability arise through the pausing and unstable
992 subthreshold oscillation mechanisms. (**b**) Analogous plot for the stochastic model containing
993 voltage-dependent noise fractions due to 1000 persistent sodium channels, and different
994 numbers of 10 pS g_{Kt} channels equivalent to the conductance indicated. Inset example
995 voltage traces (1 s of firing) : a) bottom: 101 pA, $\bar{g}_{Kt}$ 7 nS; top left: 106.7 pA, 10 nS $\bar{g}_{Kt}$; top

right: 89 pA, $\bar{g}_{Kt}$ 0.5 nS. b) bottom: 90 pA, 500 $\bar{g}_{Kt}$ channels (= 5nS); top: 95 pA, 500 $\bar{g}_{Kt}$ channels. c), d) Irregularity in simulated gap-junction-coupled ensemble of IS cells (700 g_{Kt} channels (= 7 nS), 500 NaP channels (= 5 nS)). (**c**) Cross-correlation of spike trains in one pair of neurons within a symmetrically-connected network of five IS neurons (inset), each excited by a constant stimulus of 90 pA. Exact synchrony appears as coupling is strengthened, as indicated by the single sharp peak centred on 0 ms. See Materials and methods, Spike Analysis, for details of calculation of cross-correlation. (**d**) Firing frequency, CV(ISI) and synchrony - the fraction of spikes in one cell which occur within +/- 10 ms of spikes in the other cell - as a function of the gap-junctional conductance. CV(ISI) is undiminished even for highly synchronous firing, with strong gap-junctional conductance.

Figure 8. Synchronization to oscillating inhibition is controlled by g_{Kt}. (a) Naturalistic stimulus protocol. The cell was stimulated with a constant step of AMPA conductance (g_{AMPA}, reversing at 0 mV) with added conductance Ornstein-Uhlenbeck noise (standard deviation 2% of the step amplitude, τ=5 ms), combined with a sinusoidal $GABA_A$ conductance (g_{GABA}, reversing at -60 mV) and introduction of positive, zero or negative g_{Kt}.. g_{AMPA} was adjusted so that the cell fired close to the frequency of the g_{GABA} inhibitory oscillation. **(b)** Effect of adding g_{Kt} on a slightly irregular-firing cell at 10 Hz g_{GABA}. i) Step current response (black), response to oscillatory conductance stimulus with (green) or without (blue) addition of 3.57 nS g_{Kt}. ii) Spike entrainment synchrony (see Materials and methods, Spike Analysis) to the 10 Hz g_{GABA} oscillation as a function of the oscillation amplitude. Synchrony rises progressively with oscillation amplitude in control (blue), and is depressed by addition of 3.57 nS g_{Kt} (green). iii) Spike phase histogram for pooled responses to lower amplitude g_{GABA} oscillations (up to 1 nS), showing a reduction in the sharpness of synchrony. **(c)** Example of subtracting g_{Kt} in another irregular-firing cell at 10 Hz g_{GABA}. i) example responses. ii) Subtraction of g_{Kt} (red) increased synchrony to g_{GABA} oscillation over a wide range of amplitudes, when compared to control (blue). iii) spike phase histograms for pooled responses up to 1 nS g_{GABA} oscillations. Subtraction of g_{Kt} enhances the phase preference. **d**) Lack of effect of g_{Kt} on synchronization to 40 Hz (gamma) oscillation. **e**) Summary of effects of g_{Kt} perturbation on synchrony in different cells. Each symbol denotes an experiment on an individual cell, showing the ratio of synchrony, evaluated at ≈1/3 of the maximum g_{GABA} amplitude applied in each case, during g_{Kt} injection, normalized to its control value with no injection. 10 Hz: g_{Kt} addition (n=10, green) and subtraction, (n=10, red); 40 Hz: g_{Kt} addition (n=6, green) or subtraction (n=7, red). At 10 Hz, but not 40 Hz, g_{Kt} perturbation has a

significant effect. Wilcoxon nonparametric rank sum test, p = 6.5 x 10^{-5} for both positive and negative g_{Kt}, and p = 0.36 and 0.69 at 40Hz for positive and negative g_{Kt} respectively.

FIGURE SUPPLEMENT LEGENDS

Figure 2 – figure supplement 1. Significance testing of recurrence and determinism of interspike interval sequences. a) Example cross-recurrence plot for the response to one 30 s current step trial against that of the subsequent trial. Threshold (ε) = σ_{ISI}, embedding dimension m=4. Each point coloured black denotes where sequences of 4 ISIs in each of the two trials were closer than ε to each other. b) random shuffling of both sets of ISIs results in a loss of recurrence (proportion of black points in the matrix) and determinism (fraction of black points within diagonals of length 2 or greater. c) Distribution of the recurrence values (each of which is the mean over 7 successive pairwise comparisons of consecutive 10 s trials during stationary firing) for 1,000 shuffled surrogates (each ISI sequence in the CRP is randomly permuted), compared to the actual corresponding measured recurrence level (indicated by vertical dotted gray line) over the same set of trials. d) the same for the determinism (fraction of recurrent points lying within diagonals of length >=2). A z-test (Matlab `ztest`, right-tailed) confirms that both recurrence (p<7.52e-9) and determinism (p<0.023) are significant in this case.

Figure 4 – figure supplement 1. Irregularity is not diminished by buffering intracellular calcium. An IS cell recorded with a patch pipette containing normal intracellular solution and stimulated with a steady current stimulus of 150 pA (left) is then repatched with a pipette containing intracellular solution, to which 10 mM BAPTA, a fast calcium and high-affinity buffer has been added (right), and stimulated with the same current level. Control CV(ISI) = 0.22 (125 ISIs), BAPTA CV(ISI) = 0.44 (129 ISIs, excluding initial 700 ms transient responses).

Figure 4 – figure supplement 2. Fast inactivating outward current is insensitive to TEA (2mM). Voltage steps to -10 mV from -80 mV holding potential (n=6).

1059
1060 **Figure 4 – figure supplement 3**. *Gad2*-GFP cortical interneurons from primary cultures
1061 display the two conductances required for spiking irregularity. **(a)** Cells expressed a large
1062 fast-inactivating outward current (n=4)**.** Steps from -75mV to 0mV, held at -80mV **(b)** In
1063 some cases (n=3), after measuring spike irregularity, cells were repatched with a Cs based
1064 solution and locally perfused with Cd, TEA and 4AP, to block K^+ and Ca^{2+} currents. Slow
1065 ramp depolarization (from -80 to -10, 20mV/s) revealed persistent sodium current activating
1066 approximately at -55mV, as in the slice preparation.

1067

1068 **Figure 5 – figure supplement 1.** Injecting a shunting conductance at the soma, causing a
1069 large reduction in input resistance, modifies the action potential amplitude and shape, and
1070 divides down membrane potential fluctuations, but does not regularize firing. (**a**) Top:
1071 example of control spiking during a 45 pA current step. A linear conductance of 2 nS,
1072 reversing at -70 mV was applied during the lower trace (red), and stimulus current increased
1073 to 115 pA to produce an equal firing frequency. CV in the control, calculated over 97 ISIs in
1074 repeated trials and excluding initial 400 ms of responses, was 0.46. CV with the shunting
1075 conductance, was similar, at 0.385 (195 ISIs). (**b**) Overlaid averaged action potentials, with
1076 (red) and without (black) the shunting conductance.

1077

1078 **Figure 5 – figure supplement 2.** Example spike patterns for three different cells with (a)
1079 negative g_{Kt} conductance injection and three different cells with (b) positive g_{Kt} injection,
1080 showing decreased and increased irregularity respectively.

1081

1082 **Figure 5 – figure supplement 3.** Effect of pharmacological block of A-type current in IS
1083 cells is consistent with the effect of negative g_{Kt} injection. **(a)** When 4-AP was locally
1084 perfused at 200 or 50 μM, the CVISI decreased by 44% (n=5), while PhTX 5 μM caused a
1085 mean 23% reduction (**b**, n=3).

1086

1087 **Figure 6 – figure supplement 1.** Statistics and significant recurrence and determinism of
1088 time series generated by the computational model. (**a**) Example ISI distribution for the

stochastic model, with 700 g_{Kt} channels, 500 NaP channels, and stimulus current of 83 pA. Note similarity to experimental ISI distribution (Figure 1dii). (**b**) Example cross-recurrence plot between two step depolarizations of the biophysical model with a small level of stochastic channel conductance (40 pS NaP, 30 pS g_{Kt}). (**c**) Level of recurrence, indicated by the dashed line, was significantly higher ($p < 1.3 \times 10^{-13}$, z-test) than the distribution of recurrence when one time series in each comparison was randomly shuffled (histogram). (**d**) Level of determinism was similarly higher than that of randomly-shuffled surrogates ($p < 9.3 \times 10^{-5}$). As the level of stochasticity is increased, the significance of both recurrence and determinism diminishes. Stimulus consisted of 96 pA steps lasting 20 s, total number of ISIs was 10,099, average firing frequency = 10.1 Hz, CV(ISI) = 0.22. See Materials and methods for details of analysis.

SUPPLEMENTARY DATA, RICH MEDIA AND CODE

Figure 2 Source Data File 1

Figure 2 Source Data File 2.

Figure 4 Source Data File.

Figure 5 Source Data File.

Figure 8 Source Data File.

Video 1. Movie showing dynamics in phase space of the deterministic model. Corresponds to the trajectory shown in Figure 6b.

Source Code for Model in Figures 6 and 7.

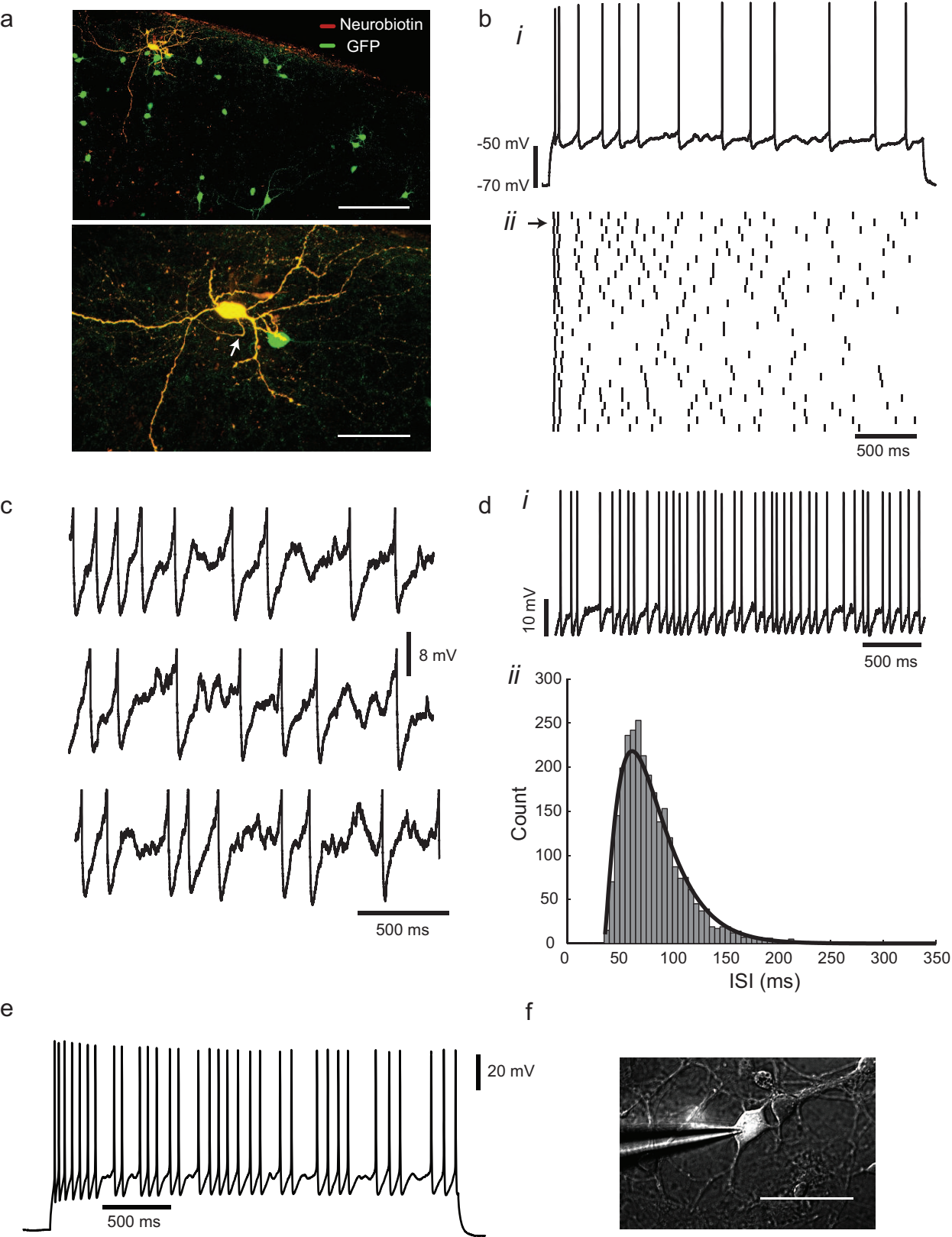
a
Neurobiotin
GFP
b
i
-50 mV
-70 mV
ii
500 ms
c
8 mV
500 ms
d
i
10 mV
500 ms
ii
Count
ISI (ms)
e
20 mV
500 ms
f

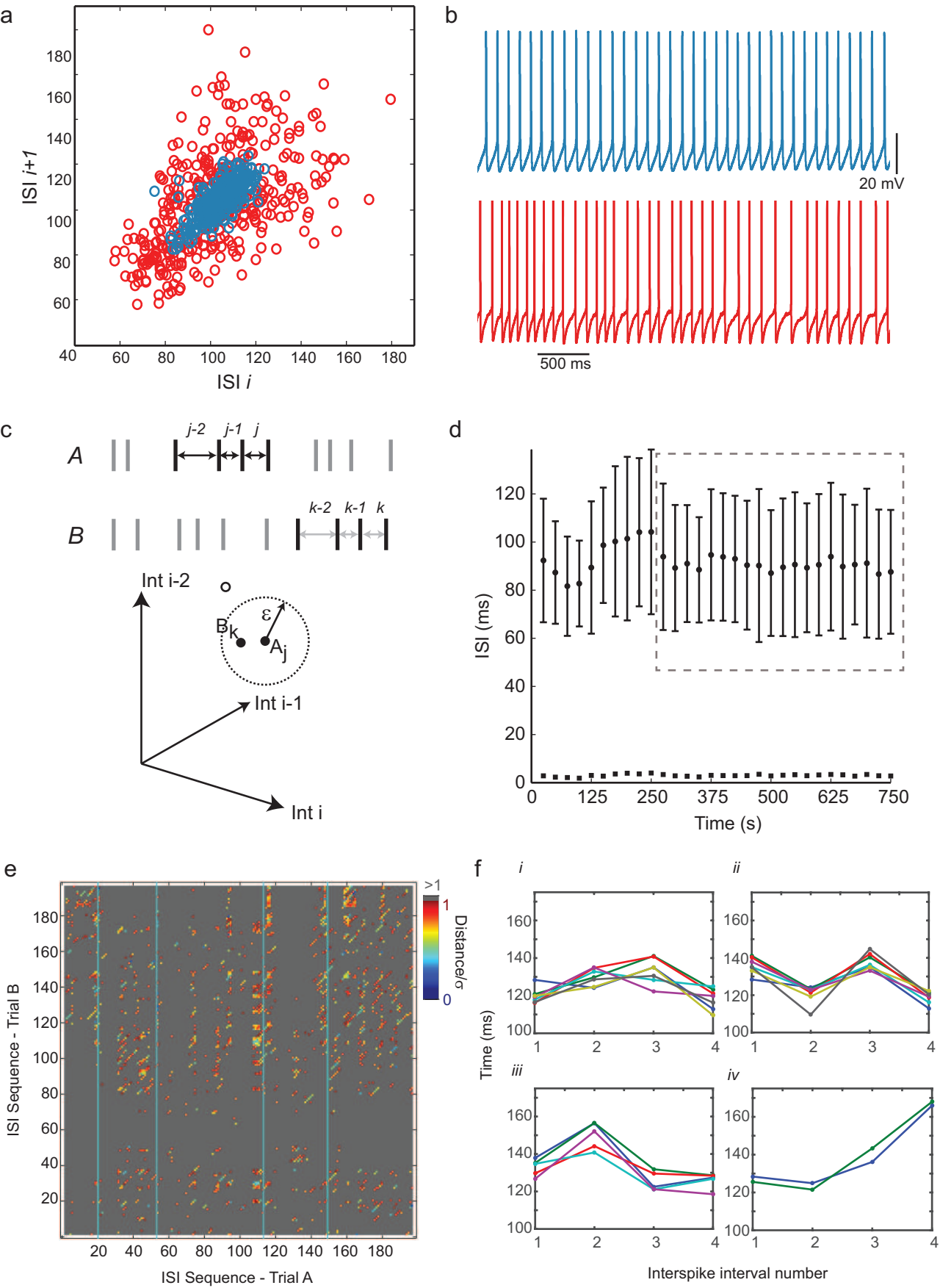
a
ISI i+1
ISI i
b
20 mV
500 ms
c
A
B
j-2
j-1
j
k-2
k-1
k
Int i-2
Int i-1
Int i
ε
B_k
A_j
d
ISI (ms)
Time (s)
e
ISI Sequence - Trial B
ISI Sequence - Trial A
Distance/σ
>1
f
i
ii
iii
iv
Time (ms)
Interspike interval number

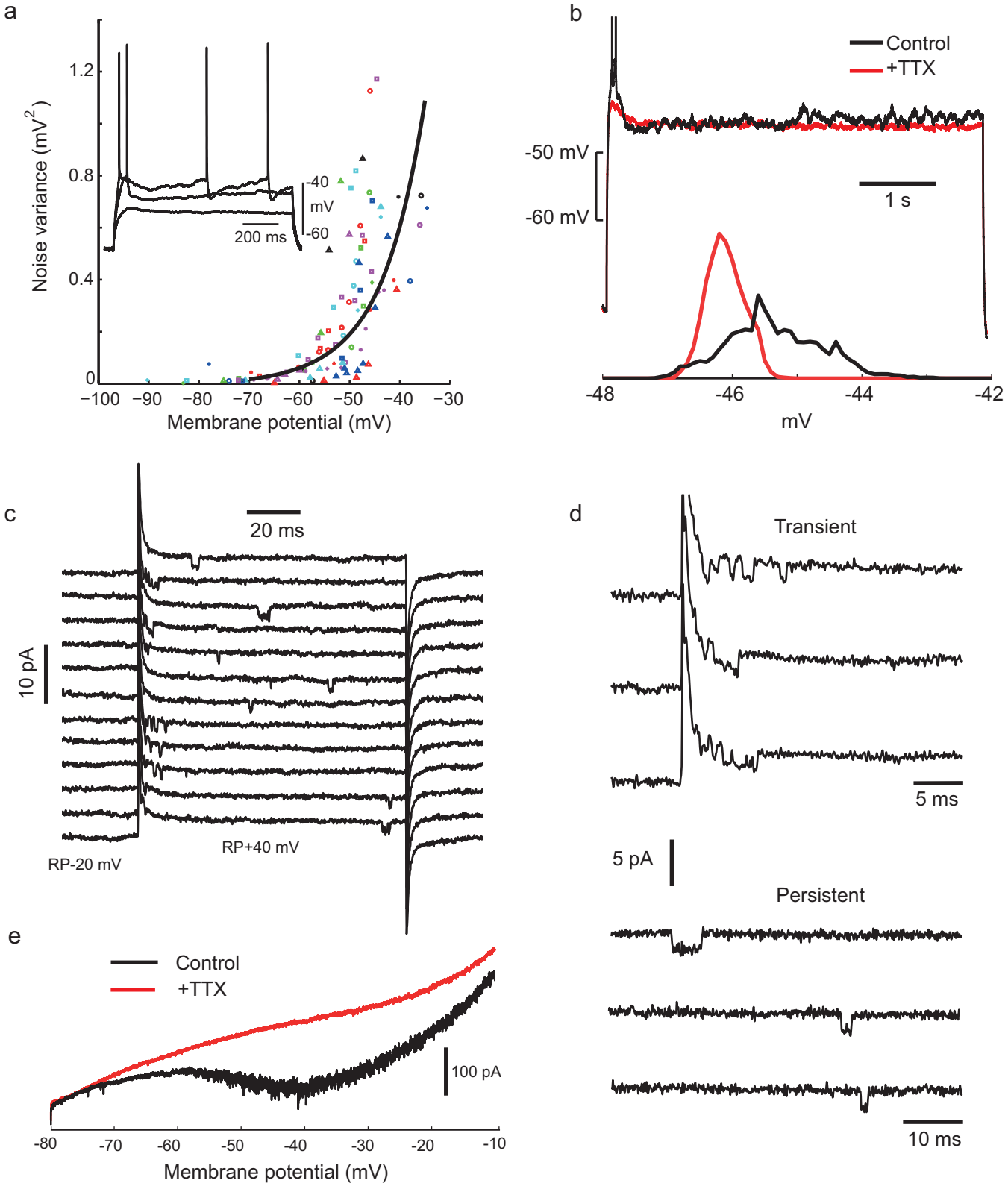
a
Noise variance (mV^2)
1.2
0.8
0.4
0
−100 −90 −80 −70 −60 −50 −40 −30
Membrane potential (mV)
-40
mV
-60
200 ms
b
Control
+TTX
-50 mV
-60 mV
1 s
-48 -46 -44 -42
mV
c
20 ms
10 pA
RP-20 mV
RP+40 mV
d
Transient
5 ms
5 pA
Persistent
10 ms
e
Control
+TTX
100 pA
-80 -70 -60 -50 -40 -30 -20 -10
Membrane potential (mV)

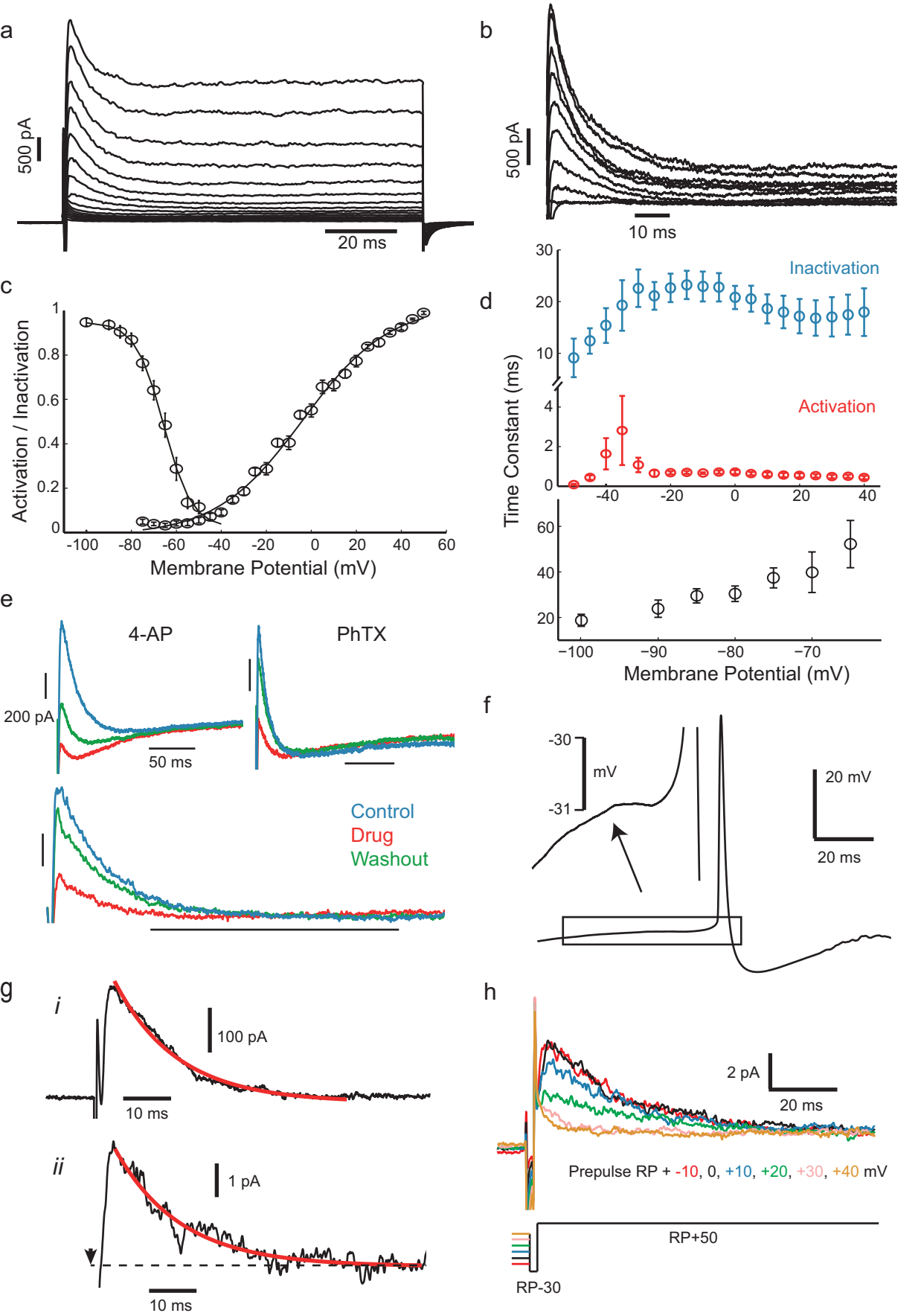
a
500 pA
20 ms
b
500 pA
10 ms
c
Activation / Inactivation
Membrane Potential (mV)
d
Inactivation
Activation
Time Constant (ms)
Membrane Potential (mV)
e
4-AP
PhTX
200 pA
50 ms
Control
Drug
Washout
f
-30
-31
mV
20 mV
20 ms
g
i
100 pA
10 ms
ii
1 pA
10 ms
h
2 pA
20 ms
Prepulse RP + -10, 0, +10, +20, +30, +40 mV
RP+50
RP-30

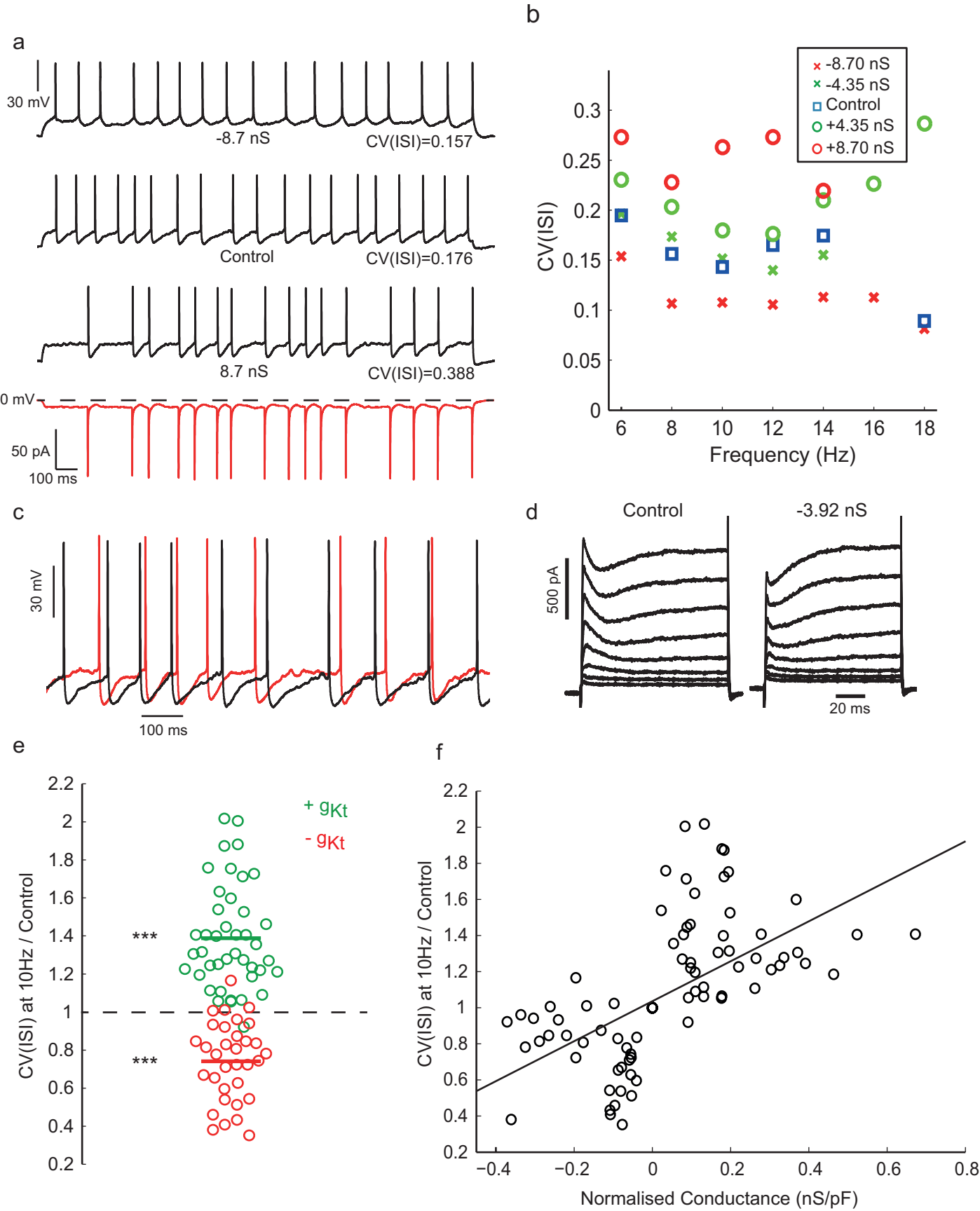
a
30 mV
-8.7 nS
CV(ISI)=0.157
Control
CV(ISI)=0.176
8.7 nS
CV(ISI)=0.388
0 mV
50 pA
100 ms
b
-8.70 nS
-4.35 nS
Control
+4.35 nS
+8.70 nS
CV(ISI)
Frequency (Hz)
c
30 mV
100 ms
d
Control
-3.92 nS
500 pA
20 ms
e
+ gKt
- gKt
CV(ISI) at 10Hz / Control
***
***
f
CV(ISI) at 10Hz / Control
Normalised Conductance (nS/pF)

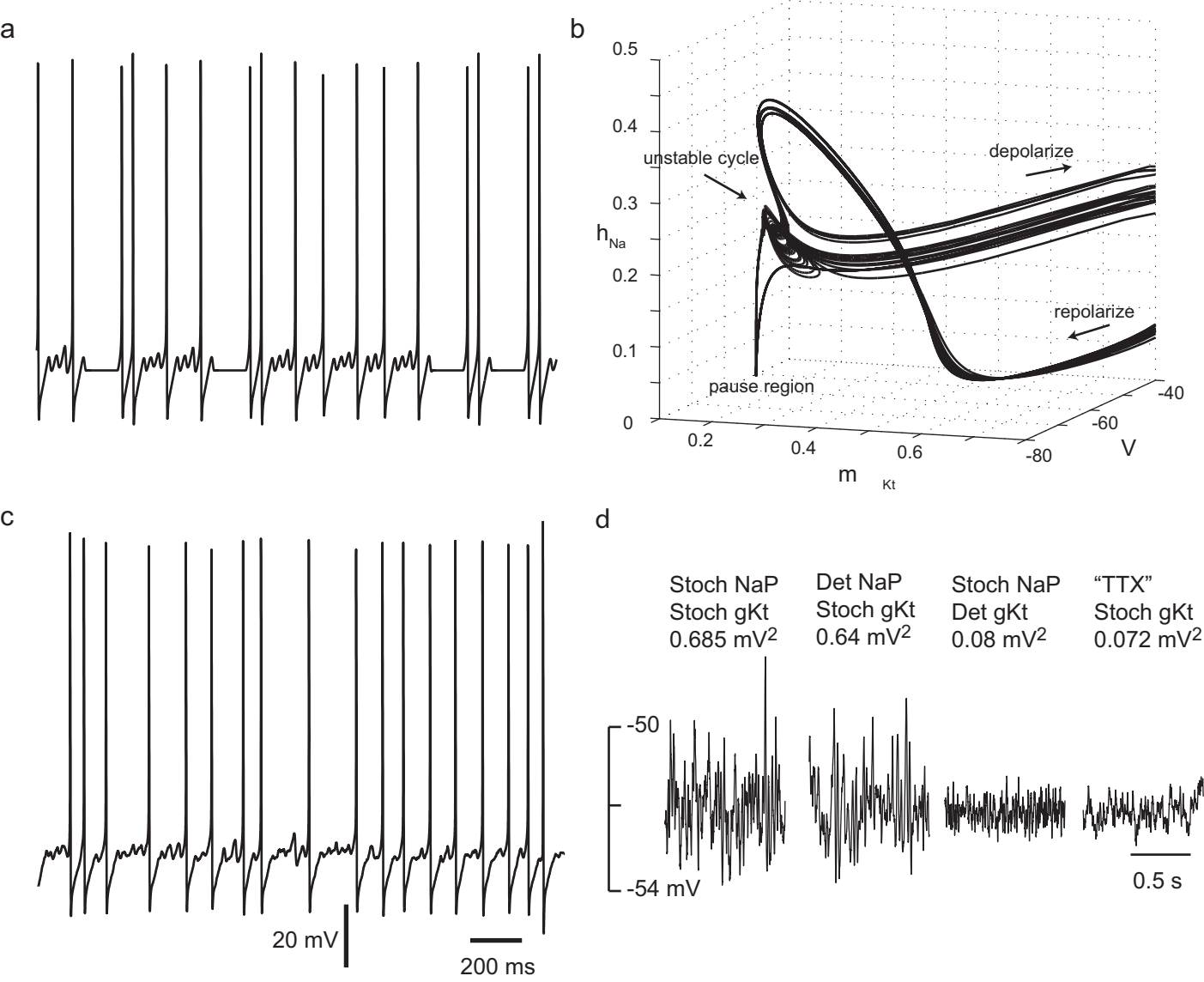
a
b
0.5
0.4
0.3
0.2
0.1
0
h_{Na}
unstable cycle
depolarize
repolarize
pause region
0.2
0.4
0.6
m_{Kt}
-40
-60
-80
V
c
20 mV
200 ms
d
Stoch NaP
Stoch gKt
0.685 mV^2
Det NaP
Stoch gKt
0.64 mV^2
Stoch NaP
Det gKt
0.08 mV^2
"TTX"
Stoch gKt
0.072 mV^2
-50
-54 mV
0.5 s

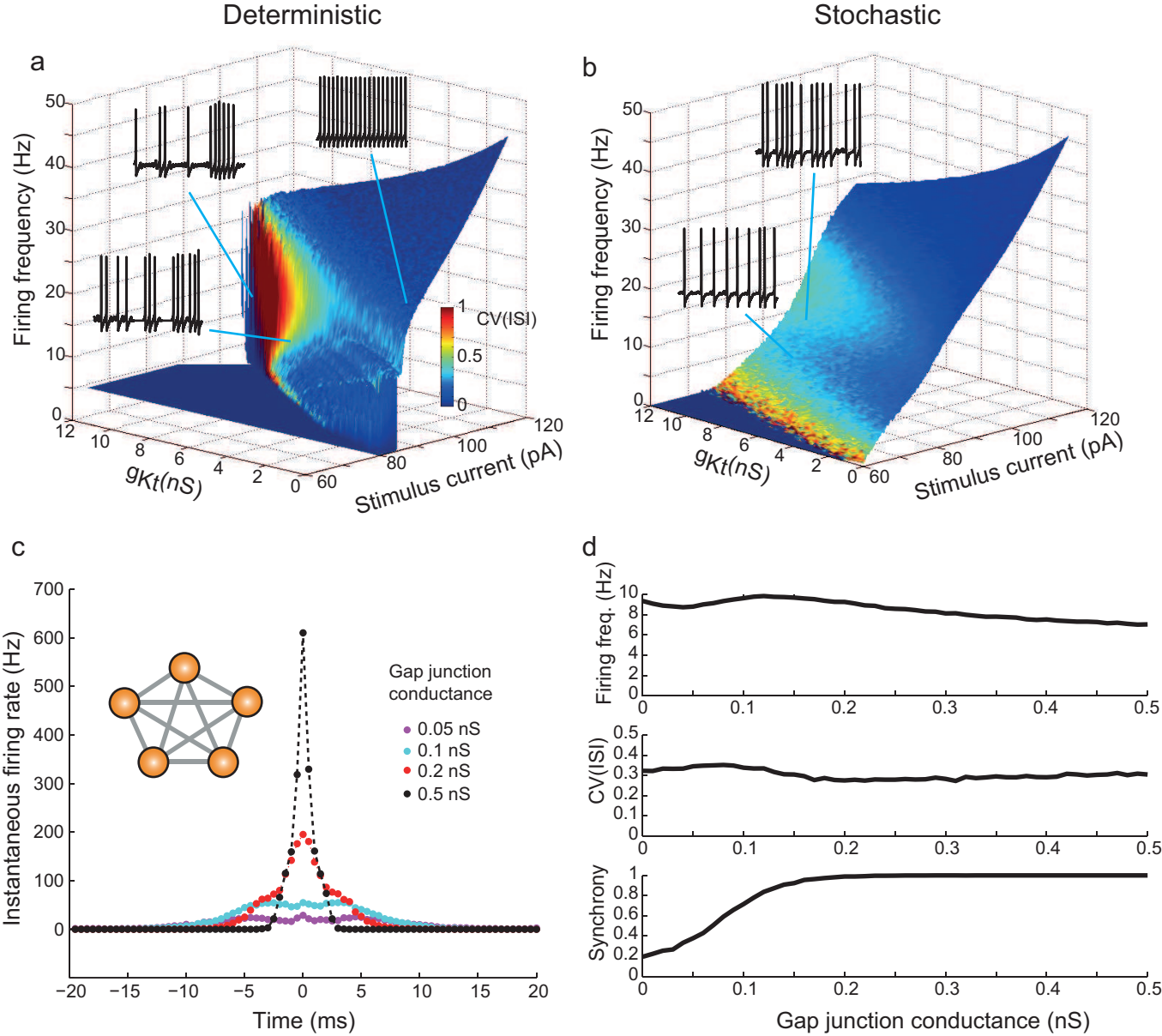
Deterministic
Stochastic
a
b
Firing frequency (Hz)
CV(ISI)
$g_{Kt(nS)}$
Stimulus current (pA)
c
d
Instantaneous firing rate (Hz)
Time (ms)
Gap junction conductance
0.05 nS
0.1 nS
0.2 nS
0.5 nS
Firing freq. (Hz)
CV(ISI)
Synchrony
Gap junction conductance (nS)

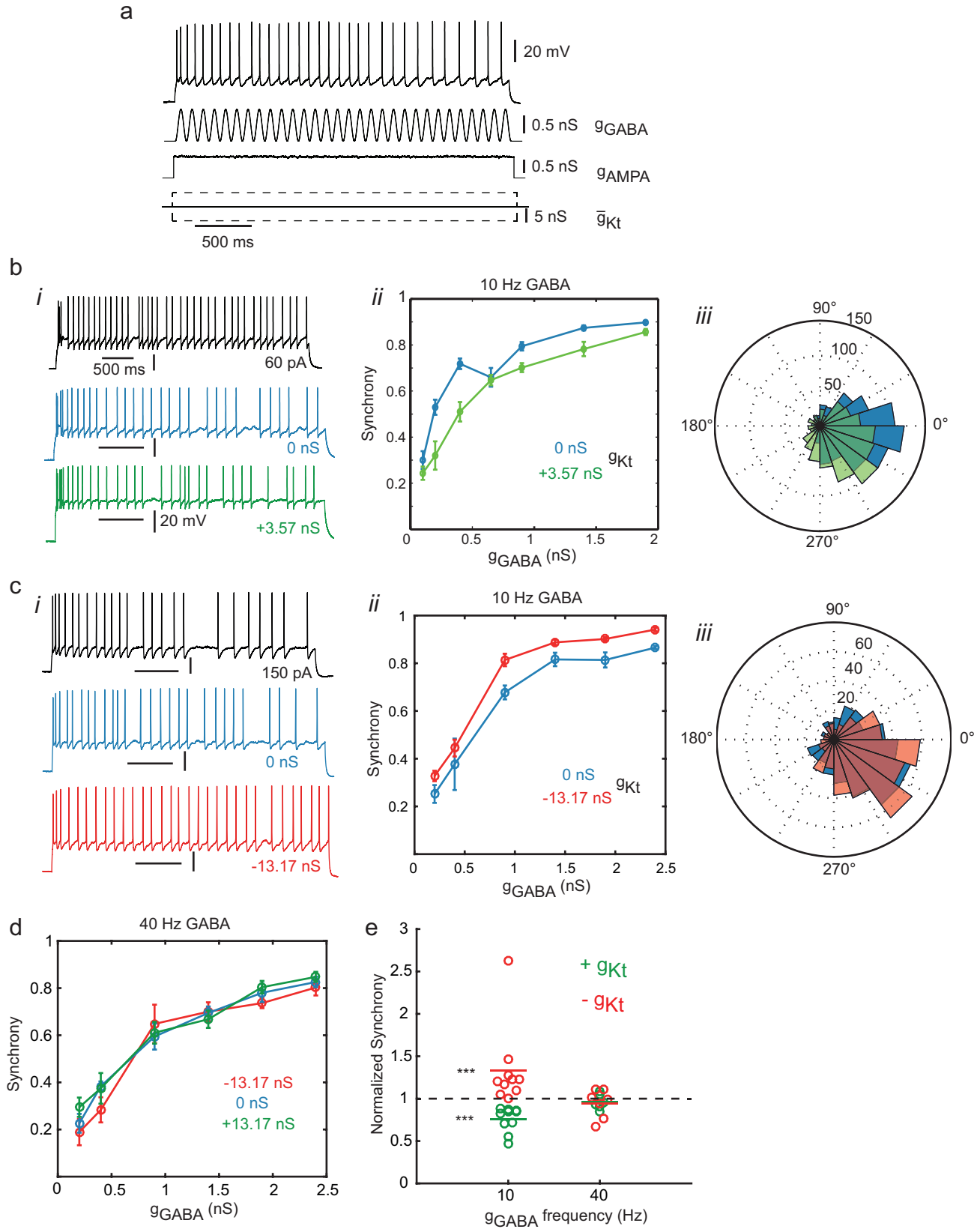
a
20 mV
0.5 nS
gGABA
0.5 nS
gAMPA
5 nS
ḡKt
500 ms
b
i
500 ms
60 pA
0 nS
20 mV
+3.57 nS
ii
10 Hz GABA
Synchrony
0 nS
+3.57 nS
gKt
gGABA (nS)
iii
90°
150
100
50
180°
0°
270°
c
i
150 pA
0 nS
-13.17 nS
ii
10 Hz GABA
Synchrony
0 nS
-13.17 nS
gKt
gGABA (nS)
iii
90°
60
40
20
180°
0°
270°
d
40 Hz GABA
Synchrony
-13.17 nS
0 nS
+13.17 nS
gGABA (nS)
e
Normalized Synchrony
+ gKt
- gKt
***
***
gGABA frequency (Hz)